Effects of physical and geochemical heterogeneities on mineral transformation and biomass accumulation during biostimulation experiments at Rifle, Colorado

Li Li [*],[1], Carl I. Steefel, Michael B. Kowalsky, Andreas Englert [2], Susan S. Hubbard

Lawrence Berkeley National Laboratory, Earth Sciences Division, 1 Cyclotron Road, MS 90-1116, Berkeley, CA 94720, United States

ARTICLE INFO

ABSTRACT

Electron donor amendment for bioremediation often results in precipitation of secondary minerals and the growth of biomass, both of which can potentially change flow paths and the efficacy of bioremediation. Quantitative estimation of precipitate and biomass distribution has remained challenging, partly due to the intrinsic heterogeneities of natural porous media and the scarcity of field data. In this work, we examine the effects of physical and geochemical heterogeneities on the spatial distributions of mineral precipitates and biomass accumulated during a biostimulation field experiment near Rifle, Colorado. Field bromide breakthrough data were used to infer a heterogeneous distribution of hydraulic conductivity through inverse transport modeling, while the solid phase Fe(III) content was determined by assuming a negative correlation with hydraulic conductivity. Validated by field aqueous geochemical data, reactive transport modeling was used to explicitly keep track of the growth of the biomass and to estimate the spatial distribution of precipitates and biomass. The results show that the maximum mineral precipitation and biomass accumulation occurs in the vicinity of the injection wells, occupying up to 5.4 vol.% of the pore space, and is dominated by reaction products of sulfate reduction. Accumulation near the injection wells is not strongly affected by heterogeneities present in the system due to the ubiquitous presence of sulfate in the groundwater. However, accumulation in the down-gradient regions is dominated by the iron-reducing reaction products, whose spatial patterns are strongly controlled by both physical and geochemical heterogeneities. Heterogeneities can lead to localized large accumulation of mineral precipitates and biomass, increasing the possibility of pore clogging. Although ignoring the heterogeneities of the system can lead to adequate prediction of the average behavior of sulfate-reducing related products, it can also lead to an overestimation of the overall accumulation of iron-reducing bacteria, as well as the rate and extent of iron reduction. Surprisingly, the model predicts that the total amount of uranium being reduced in the heterogeneous 2D system was similar to that in the 1D homogeneous system, suggesting that the overall uranium bioremediation efficacy may not be significantly affected by the heterogeneities of Fe(III) content in the down-gradient regions. Rather, the characteristics close to the vicinity of the injection wells might be crucial in determining the overall efficacy of uranium bioremediation. These findings have important implications not only for uranium bioremediation at the Rifle site and for bioremediation of other redox sensitive contaminants at sites with similar characteristics, but also for the development of optimal amendment delivery strategies in other settings.

* Corresponding author.
  E-mail address: lili@eme.psu.edu (L. Li).
[1] Now at The Pennsylvania State University, Department of Energy and Mineral Engineering, United States.
[2] Now at Ruhr University Bochum, Applied Geology Department, Universitaetsstr. 150, 44801 Bochum, Germany.

1. Introduction

Contamination by redox-sensitive chemicals, including radionuclides, chlorinated hydrocarbons, organic acids, and complexing agents is a growing environmental concern. Bioremediation, which involves injection of organic carbon as electron donors into the subsurface to stimulate indigenous bacteria to transform contaminants into less toxic or less mobile forms, shows promise for treating plumes in the subsurface created by such contaminants. Although it has been shown that many bacteria, including the Fe(III)-reducing bacteria (FeRB) and sulfate-reducing bacteria (SRB), are able to reduce contaminants in laboratory systems (Lovley and Phillips, 1992; Lovley et al., 1991), bioremediation at the field scale faces many challenges.

The potential for bioremediation-induced pore clogging is one such challenge. The injection of organic carbon often leads to many biogeochemical reactions, the products of which can react to form secondary mineral precipitates and low-solubility gases. In addition, the growth of bacteria can result in the accumulation of bacterial cell bodies and extracellular polymer substance (EPS) (Baveye et al., 1998; Molins and Mayer, 2007). These reaction products can clog pore bodies and pore throats, thereby potentially changing the flow direction and the efficacy of bioremediation. Laboratory experimental studies have observed mineral precipitates, biomass accumulation, as well as the resulting changes in porosity and hydraulic conductivity (Cunningham et al., 1991; Seki et al., 2006; Taylor and Jaffe, 1990a,b). Field experiments have documented changes in tracer test recoveries over time, which may also be due to pore clogging processes (Faybishenko et al., 2008; Wu et al., 2006). As such, it is important to quantitatively estimate the amount of precipitates and biomass so that the possible effects of pore clogging can be assessed.

Another challenge in applying bioremediation at the field scale is the uncertainty and complexity in the intrinsic heterogeneities of contaminated sites. Physical properties, such as porosity and hydraulic conductivity, and geochemical properties, such as the abundance of reacting minerals, show significant spatial variations in the subsurface (Gelhar, 1993). Physical heterogeneities have long been known to affect flow and transport processes (Dagan, 1990; Freeze, 1975; Gelhar and Axness, 1983; Zinn et al., 2004), while the effect of geochemical (or mineralogical) heterogeneities on reactive transport processes has only been recognized more recently (Glassley et al., 2002; Li et al., 2006, 2007a,b; Meile and Tuncay, 2006; Scheibe et al., 2006; Tompson et al., 1996). Both types of heterogeneities can profoundly affect bioremediation processes, which require the co-occurrence of multiple reacting agents, including the electron donor, the electron acceptor, and the biomass. The level of co-occurrence is very much affected by the complex interactions between hydrological, geochemical, and biological processes that occur simultaneously under field conditions, and by the effects of heterogeneities on these processes. For example, the spatial variations in hydraulic conductivity (physical heterogeneity) determine the flow and transport of injected electron donors. The electron acceptors and bacteria, however, do not necessarily reside in the flow paths of the electron donors. As such, the physical and geochemical heterogeneities determine the

level of interactions among reacting agents and the spatial distribution of reaction products, both of which can largely determine the degree of pore clogging that may occur.

Despite the importance of porous medium heterogeneities in controlling reactive transport processes during bioremediation, full characterization of field sites with high resolution is daunting and cost prohibitive, if not impossible. As such, we frequently face the challenge of inferring the spatial distribution of physical and geochemical properties from limited data, a task which is inevitably made difficult due to uncertainty and non-uniqueness (de Marsily et al., 2005).

This work aims to understand the effects of physical and geochemical heterogeneities on the mineral transformation and biomass accumulation that potentially occurred during a field biostimulation experiment designed for uranium bioremediation in Rifle, Colorado. The uranium-contaminated Rifle site was formerly a uranium ore processing facility and is now a U.S. Department of Energy (DOE) Integrated Field Research Challenge (IFRC) site. It has been the subject of several biostimulation experiments (Anderson et al., 2003; Yabusaki et al., 2007) that involved the injection of acetate as an electron donor to react primarily with three competing electron acceptors: U(VI), Fe(III), and sulfate. There is evidence of uneven delivery of bromide (used as a non-reactive tracer) and acetate in both the horizontal and vertical directions, which has been speculated to be due to spatial variations in hydraulic conductivity, as well as microbiological and geochemical heterogeneity at the site (Vrionis et al., 2005). It is believed that the SRB at the site do not reduce and immobilize U(VI); rather, it is likely that the FeRB (dominated by members of the family *Geobacteraceae*) are primarily responsible for transforming the mobile U(VI) to immobile U(IV) (Anderson et al., 2003).

Early modeling of the Rifle field experiment was performed using relatively simple geochemistry (Yabusaki et al., 2007). Subsequently, we performed additional work that substantially improved reproduction of the field geochemistry data using a full reaction network. The reaction network was developed based on column and field experiments and incorporated the growth of biomass in the reaction rate expression (Li et al., 2009). Our model in some cases provides an improved fit of the breakthrough curves. Our study indicated that products of microbially mediated reactions form mineral precipitates, possibly including $CaCO_3$, $MgCO_3$, $FeCO_3$, amorphous FeS, elemental sulfur, and $UO_2(s)$, as depicted in Fig. 1. In addition, these reactions can lead to the accumulation of biomass in the form of both FeRB and SRB.

In this study, we use reactive transport modeling based on the previously-developed reaction network (Li et al., 2009) to assess the effects of physical and geochemical heterogeneities on the temporal and spatial patterns of mineral precipitates and biomass. The spatial distribution of hydraulic conductivity was obtained through inverse modeling of the Br^- breakthrough data. Based on geochemical analysis of Fe(III) content associated with different fractions of the Rifle sediments, we then assumed a negative correlation between hydraulic conductivity and Fe(III) content to obtain a spatial distribution of Fe(III) content. Using these spatial distributions as input, the reactive transport model CrunchFlow (Steefel and Maher, 2009) was then used to simulate the transport and biogeochemical processes that occurred during
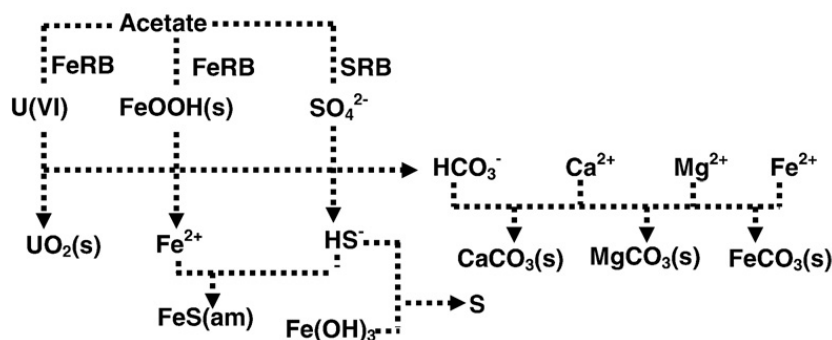
Fig. 1. Important kinetically controlled reactions and the formation of mineral precipitates and biomass during bioremediation at the Rifle site. Other instantaneous reactions that are considered at equilibrium (including aqueous speciation and ion exchange) are not shown.

the biostimulation experiment. Based on a good fit of the modeling output to the field aqueous geochemistry data measured during the experiment, the amounts of mineral precipitates and biomass were estimated. To the best of our knowledge, this study is the first to assess the role of physical and geochemical heterogeneities in determining the spatial and temporal evolution of reaction products, utilizing tracer data and aqueous geochemistry and mineral characterization data to constrain the model.

The remainder of this paper is organized as follows. Section 2 will describe the field experiment and characteristics of the site. Section 3 will describe the methods for generating the hydraulic conductivity and Fe(III) content fields, and the reactive transport modeling approach. Section 4 will describe the results, and conclusions will be drawn in Section 5.

2. Rifle IFRC site and the 2002/2003 biostimulation experiments

Shallow groundwater at the Old Rifle site is contaminated with uranium at the micromolar (~0.2–0.4 ppm) level, although a much larger inventory exists in a sorbed form. Besides uranium, other important species such as Ca^{2+}, Mg^{2+}, SO_4^{2-}, and HCO_3^-, also exist in the groundwater, as listed in Table 1. Where direct analyses are unavailable (as in the case of dissolved Fe(III)

Table 1
Initial and boundary conditions for the primary aqueous species.

Species	Concentration (M)	Ways obtained
pH	7.0	Measured
Fe^{2+}	4.0×10^{-5}	Measured
Fe^{3+}	4.3×10^{-12}	Equilibrium with goethite
Na^+	8.2×10^{-3}	Measured
K^+	1.9×10^{-4}	Measured
Acetate	1.0×10^{-8}	Measured as "not detected"
Br^-	1.0×10^{-8}	Measured as "not detected"
$CO_2(aq)$	4.7×10^{-3}	Equilibrium with calcite
SiO_2 (aq)	3.8×10^{-4}	Equilibrium with quartz
$O_2(aq)$	1.6×10^{-5}	Measured
Ca^{2+}	5.1×10^{-3}	Measured
Mg^{2+}	5.1×10^{-3}	Measured
SO_4^{2-}	7.5×10^{-3}	Measured
HS^-	4.0×10^{-14}	Measured as "not detected"
UO_2^{2+}	1.0×10^{-6}	Measured
NH_4^+	1.0×10^{-3}	Measured
NO_3^-	1.0×10^{-4}	Measured as "not detected"
Cl^-	1.1×10^{-2}	Charge balanced

concentrations), the constraint used to determine the concentration for the purposes of modeling is given. The groundwater flows mainly within a gravelly sandy aquifer dominated by alluvium, with an average hydraulic conductivity of approximately 35 m/day and a mean porosity of 0.27 (Anderson et al., 2003). The sediments include both coarse-grained materials (gravels and cobbles) and fine-grained silt and clay. The minerals present in the sediments include quartz, calcite, clays (kaolinite, smectite, and illite), and various iron-containing minerals (goethite, hematite, magnetite, and ferrihydrite). As a result, both physical and geochemical properties (including an abundance of Fe-oxyhydroxide) vary significantly over space, depending on the character of the local sedimentary units.

The shallow unconfined aquifer of the Rifle site was subject to two successive uranium field experiments in 2002 and 2003, lasting 119 and 111 days, respectively. A plan view of the wells at the site, together with the hydraulic conductivity and Fe(III) content fields (described below), is shown in Fig. 2. During the experiments, acetate and bromide were mixed with background groundwater and injected into the subsurface through 20 fully penetrating injection wells aligned (approximately) perpendicular to the direction of major groundwater flow. Three control wells were located up-gradient of the injection wells, and three rows of monitoring wells (15 in total) were located down-gradient from the injection gallery. During the field experiments, aqueous geochemical data, including pH, concentrations of acetate, Br^-, Fe(II), S(−II), SO_4^{2-}, and U(VI), were collected periodically from the background and monitoring wells and analyzed to detect changes in the aqueous geochemical conditions. Detailed information on the test site, measurements of field aqueous geochemistry before and after acetate injection, as well as characterization of the mineralogy and hydrogeology were published elsewhere (Anderson et al., 2003; Yabusaki et al., 2007).

Upon acetate injection, the biogeochemistry of the contaminated site is driven by three major microbially mediated reactions: Fe(III) reduction, sulfate reduction, and uranium reduction (Fig. 2). Unlike other contaminated sites (Luo et al., 2007), it is believed that only the Fe(III)-reducing bacteria at the Rifle site can reduce uranium, while the SRB do not transform the soluble U(VI) to highly insoluble U(IV). As such, the abundance and spatial distribution of Fe(III) content become extremely important for successful bioremediation to occur.

The products of the microbially mediated reactions can lead to a variety of mineral precipitation and dissolution reactions.
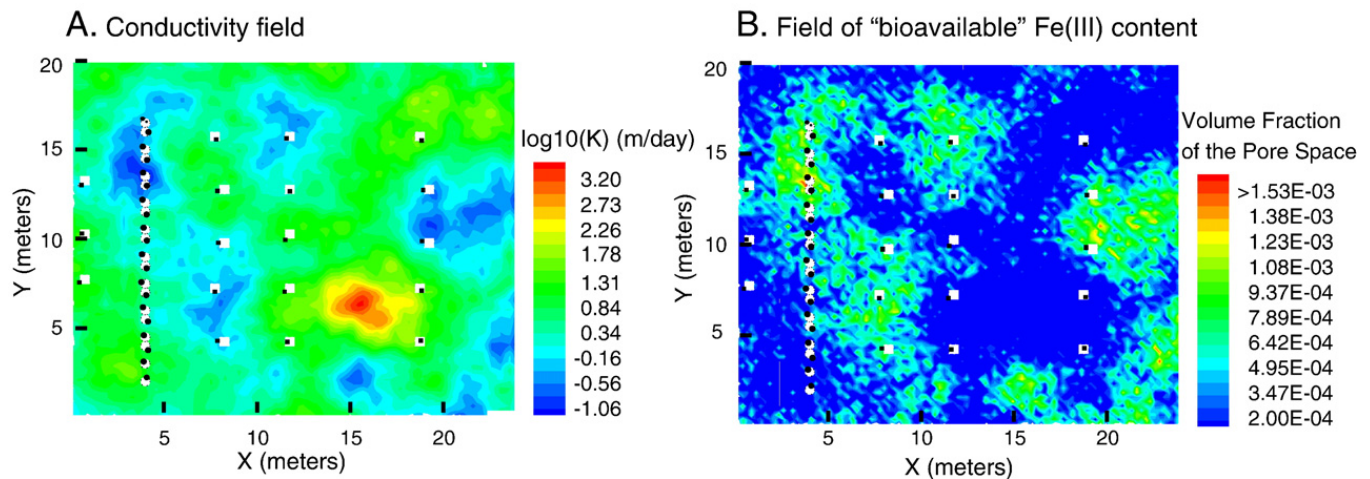
Fig. 2. Plan view, depth-averaged spatial distributions of hydraulic conductivity and bioavailable iron content used for the reactive transport modeling. Also shown are the background wells (first black-white column from the left), injection wells (second column from the left), and monitoring wells (column 3-5 from the left).

For example, bicarbonate generated from all three bioreduction reactions can react with Ca^{2+} in the groundwater to form calcite. The Fe(II) generated from iron reduction can react with the S($-$II) produced by sulfate reduction to form amorphous FeS. In addition, the biogeochemical reactions can also result in the accumulation of cell bodies of FeRB and SRB, as well as extracellular polymer substance (EPS). All these reaction products have the potential for reducing and clogging the pore space.

3. Methodology

3.1. Inverse modeling to obtain heterogeneous hydraulic conductivity fields

The Br^- concentrations in the down-gradient monitoring wells show highly complex breakthrough curves that are influenced by subsurface heterogeneity, the reported time-varying injection rate, and the fluctuating water table. We performed inverse modeling of the Br^- concentration data in order to characterize the physical heterogeneity at the site, specifically the hydraulic conductivity. While details are given elsewhere (Englert et al., in preparation), a brief overview of the inverse modeling procedure is provided in this section to provide context for subsequent results.

To simulate the bromide distribution, a depth-averaged two-dimensional flow and transport model was developed using TOUGH2 (Pruess et al., 1999) to simulate the field experiment. The hydraulic head gradient of the background groundwater was assumed to be constant and equal to 0.004 m/m, and the main direction of regional groundwater flow was assumed perpendicular to the plane formed by the injection wells. (Note that the local gradient in the vicinity of the injection wells changes during the simulation as water is injected into the model.) The model covers a region of 25 m by 30 m, with grid spacing ranging from 0.25 m to 1 m, giving a total of 7569 grid blocks. The desired gradient was maintained by keeping the pressures (or hydraulic heads) at the up-gradient and down-gradient boundaries constant, while the tracer concentrations at the upstream boundary were fixed at zero. A zero-flux boundary condition was used for the boundaries parallel to the mean flow direction. It

should be noted that the reactive transport modeling, described below, employs a slightly different grid for simulation (the main difference being near the boundaries of the model). A linear interpolation procedure was used to map the hydraulic conductivity distribution obtained in this step onto the reactive transport modeling grid.

The code iTOUGH2 (Finsterle, 2004), which provides inverse modeling capabilities for TOUGH2, was used to estimate the parameters of interest. The inverse procedure proceeds as follows. The steady-state pressure distribution is first calculated based on an initial estimate of the unknown parameter values, and on the specified boundary conditions. This distribution, along with the tracer concentration uniformly set to zero, then serves as the initial condition for the simulation. The next stage of the simulation is then initiated as bromide and water are injected into the 20 injection wells at the rates measured in the field. Through iteration of the simulation, an optimization algorithm determines the parameter values that provide the best match between simulated and measured Br^- concentrations in the monitoring wells.

The objective of the inverse modeling is to estimate the heterogeneous hydraulic conductivity distribution, which is cast as a space random function using a geostatistical formulation employing a statistical model (semi-variogram) inferred from field data. All other parameters, including porosity, were assumed to be spatially uniform. Heterogeneous hydraulic conductivity fields are generated using Sequential Gaussian simulation (SGSIM) (Deutsch and Journel, 1992). They are conditioned to unknown values at a number of locations, called pilot points (e.g., (Gomez-Hernandez et al., 1997)), which are the parameters to be estimated through inverse modeling. In our study we defined 25 pilot points regularly spaced throughout the modeled region (Fig. 2A). An example of a related approach is provided, albeit in a different application, in other publications (Kowalsky et al., 2005; Kowalsky et al., 2004).

Lastly, note that the geostatistical nature of this inverse modeling approach normally requires that multiple inversion realizations be performed, based on a different initial random seeds, such that multiple estimates of the hydraulic conductivity field are obtained, each conditioned to the measured Br^- concentration data. However, in this paper, we focus

on a single inversion realization corresponding to the 2002 experiment. The effect of uncertainty in the estimated hydrological parameters on the reactive transport predictions is the subject of the ongoing research.

3.2. Generation of Fe(III) content fields

In addition to the hydraulic conductivity field, the spatial distribution of the Fe(III) content is needed for reactive transport modeling because FeRB play a key role in mediating uranium reduction at the Rifle site. Although the Fe(III) content was measured for a few Rifle sediments, its spatial distribution is largely unknown. As mentioned in previous sections, the Rifle sediments contain both coarse-grained and fine-grained materials. The fine-grained fractions of the sediments (clay and silts) contain much more Fe(III) than the coarse-grained materials, as shown in Table 2. The data in Table 2 represent the 0.5 N hydroxylamine–HCl extractable Fe (Lovley and Phillips, 1987), which targets amorphous iron oxide and is often taken as a measure of "bioavailable" Fe(III). It does not include Fe(III) in clays, which have been reported as one of the major sources of electron acceptor in the Rifle sediments (Komlos et al., 2007). It also does not include more crystalline oxide phases like hematite and magnetite that are not normally extractable with hydroxylamine. Meanwhile, areas with coarse-grained materials tend to have relatively larger hydraulic conductivity values compared to regions with fine-grained materials. As such, it appears reasonable to assume there is a negative correlation between the iron content and hydraulic conductivity. The spatial distribution of iron content is obtained based on this assumption, which is also consistent with observations for other soils and sediments (Barber et al., 1992; Shelobolina et al., 2004; Zachara et al., 1995).

Based on this assumption, a probability model is used to calculate the mean and variance of Fe(III) content for each specific location according to the following equations (Ross, 2000), assuming the iron content at a specific point follows Gaussian distribution truncated at zero:

$$\mu_{Fe,i} = \mu_{Fe} + \rho \frac{\sigma_{Fe}}{\sigma_{logK}} (log K_i - \mu_{log K}) \quad (1)$$

$$\sigma_{Fe,i}^2 = \sigma_{Fe}^2 (1.0 - \rho^2). \quad (2)$$

Here $\mu_{Fe,i}$ is the local mean of reactive Fe(III) content for a specific grid block i, μ_{Fe} is the global mean of Fe(III) content for the whole domain, σ_{Fe} is the global standard deviation of the Fe(III) content, $log K_i$ is the logarithm of conductivity (m/day) at the grid block i, and μ_{logK} is the global mean of $log K$, σ_{logK} is the global standard deviation of $log K$, and ρ is the correlation

coefficient between Fe(III) content and $log K$. As indicated by the two equations, the mean of the reactive Fe(III) content at specific locations ($\mu_{Fe,i}$) depends on the global means of Fe(III) content and $log K$, the correlation between the two, global standard deviations of the two, as well as the local value $log K_i$. The local variance of the Fe(III) content $\sigma_{Fe,i}^2$ is determined by the global variance of Fe(III) content σ_{Fe}^2 and the correlation coefficient. Eq. (1) calculates the local mean of the Fe(III) content at a specific grid block i, and Eq. (2) calculates the variance of Fe(III) content at a specific grid block, which determines the extent of possible variation. The combination of the two equations defines the Gaussian distribution of Fe_i. From this distribution a random number generator was used to obtain a specific value for Fe(III) content at the grid block i. The values of $\mu_{Fe,i}$ and Fe_i can be negative from random sampling. However, the model assures non-zero iron content by assigning a small value when Fe_i is negative.

Table 3 lists the probabilistic and statistical parameters used in Eqs. (1) and (2) for generation of the iron content field. Values of μ_{logK} and σ_{logK} are from the statistics of the hydraulic conductivity field. The parameters related to Fe(III) content are more uncertain. The mean Fe(III) content in the field sediments can be different from those in Table 2, which only lists the values for the portion of sediments with grain size smaller than 4 mm. The field sediments contain a large percentage of materials with grain size larger than 4 mm. As such, the mean Fe(III) content for field sediments was calculated by taking into account the percentage of >4 mm portion of the sediments. It is also assumed that the Fe(III) content per unit surface area is the same for sediments of all grain sizes. That is, the fine-grain-sized sediments contain more Fe(III) because they have larger surface areas. In this way a mean amorphous Fe(III) content was calculated to be 13.33 µmol/g. However, according to our previous study and the literature (Li et al., 2009; Roden and Zachara, 1996), not all amorphous Fe(III) is microbially reducible. Only about 8–20% of the amorphous Fe(III) is considered "bioavailable". As such, the average bioavailable iron content, μ_{Fe} is assumed to be 2.5 µmol/g. The standard deviation of the iron content is assumed to be the same as the mean. The negative correlation coefficient between hydraulic conductivity and Fe(III) content was arbitrarily chosen to be −0.8.

3.3. Reactive transport modeling

With the hydraulic conductivity and reactive iron content fields (described in previous sections), the reactive transport model CrunchFlow (Steefel and Maher, 2009) was used to simulate the biogeochemical and transport processes that occur during the bioremediation experiments and to assess

Table 2
Hydroxylamine-extractable Fe(III) content in different fractions of Rifle sediments for grain size smaller than 4 mm.

Fractions	Weight %	Fe (µmol/g) [a]
Clay (<2 µm)	0.4	187.60
Silt (2 µm < fraction < 0.4 mm)	5.0	83.18
Pebbles (>0.4 mm)	94.6	20.78
Total	100	24.58

[a] Defined by a 0.5 N hydroxylamine–HCl extraction technique (Lovley and Phillips, 1987) which targets amorphous iron oxide.

Table 3
Probabilistic and statistical parameters used to generate Fe(III) content fields.

Parameters	Values
μ_{Fe}	2.5 µmol/g
σ_{Fe}	2.5 µmol/g
μ_{logK}	0.37 m/day
σ_{logK}	0.60 m/day
ρ	−0.8

Table 4

Important reactions involved in uranium bioremediation and their kinetic and thermodynamic parameters.

#	Reaction stoichiometry	Kinetic parameters (as shown in Eq. (1))			
		k_{max} (mol/L/s/cell)	$K_{M,S}$ (mol/L)	$K_{M,TEA}$ (mol/L)	K_I (μmol/g)
	Microbially-mediated redox reactions				
1 [a]	$FeOOH(s) + 1.925H^+ + 0.033NH_4^+ + 0.208CH_3COO^- \rightarrow Fe^{2+} + 0.033C_5H_7O_2N_{(FeRB)} + 0.25HCO_3^- + 1.6H_2O$	4.74×10^{-17}	1.0×10^{-3} [d]	157.28 μmol/g [e]	–
2 [b]	$SO_4^{2-} + 1.082CH_3COO^- + 0.052H^+ + 0.035NH_4^+ \rightarrow 0.035C_5H_7O_2N_{(SRB)} + 0.104H_2O + 2HCO_3^- + HS^-$	2.78×10^{-13}	1.0×10^{-3} [f]	1.0×10^{-3} [g]	1.8 [h]
3 [c]	$UO_2^{2+} + 0.067NH_4^+ + 0.417CH_3COO^- + 0.8H_2O \rightarrow UO_2(s) + 0.0667C_5H_7O_2N_{(FeRB)} + 0.5HCO_3^- + 2.15H^+$	1.11×10^{-17}	1.0×10^{-4} [i]	1.0×10^{-6} [j]	–
	Mineral dissolution and precipitation	$\log k$ (mol/m²/s)		$\log K_{eq}$	
4	$CaCO_3(s) + H^+ \Longleftrightarrow Ca^{2+} + HCO_3^-$	-5.2		1.85	
5	$MgCO_3(s) + H^+ \Longleftrightarrow Mg^{2+} + HCO_3^-$	-5.2		2.29	
6	$Fe^{2+} + H_2S(aq) \Longleftrightarrow FeS(am) + 2H^+$	-9.0		3.50	
7	$Fe(OH)_3(s) + 0.5H_2S(aq) + 2.5H^+ \Longleftrightarrow Fe^{2+} + 0.5S(s) + H_2O + 2.00H^-$	-3.0		-19.60	
8	$FeCO_3(s) + H^+ \Longleftrightarrow Fe^{2+} + HCO_3^-$	-9.0		-0.19	
	Ion exchange (Vanselow convention)	Cation exchange capacity		$\log k$ [k]	
9	$NaX \Longleftrightarrow Na^+ + X^-$	8.0×10^{-5} eq/g		0.00	
10	$KX \Longleftrightarrow K^+ + X^-$			-0.60	
11	$CaX_2 \Longleftrightarrow Ca^{2+} + 2X^-$			-0.50	
12	$MgX_2 \Longleftrightarrow Mg^{2+} + 2X^-$			-0.40	

[a] Assuming 60% of electron equivalents in acetate are used for energy.

[b] Assuming 92% of the electron equivalents in acetate are used for energy.

[c] Assuming 60% of electron equivalents in acetate are used for energy.

[d] (Liu et al., 2001).

[e] Range between 10.5 and 235.0 μmol/g (Bonneville et al., 2004; Roden and Zachara, 1996; Van Cappellen and Wang, 1996).

[f] Range between 0.0043 and 0.1 mM (Jung et al., 1999).

[g] Range between 0.1 and 7.5 mM (Pallud and Van Cappellen, 2006; Porter et al., 2007).

[h] Range between 0.8 and 5 μmol/g (Wang et al., 2003; Yabusaki et al., 2007).

[i] No literature data available.

[j] Range between 0.0001 and 24 mM (Boonchayaanant et al., 2008; Wang et al., 2003).

[k] All logK values from (Charlet and Tournassat, 2005).

the effects of physical and geochemical heterogeneities on mineral precipitation and biomass accumulation. CrunchFlow solves equations of mass conservation, momentum conservation, and energy conservation, and has been used to understand many reactive transport systems (Giambalvo et al., 2002; Knauss et al., 2005; Maher et al., 2006). For mass conservation, reactive transport models usually partition aqueous species into primary and secondary species (Lichtner, 1985) and the equations of mass conservation are written for primary species. The following is a representative mass conservation equation for a specific primary species i:

$$\frac{\partial(\phi C_i)}{\partial t} = \nabla(\phi D_i \nabla C_i) - \nabla(\phi u C_i) - \sum_{r=1}^{N_r} \nu_{ir} R_r - \sum_{m=1}^{N_m} \nu_{im} R_m. \quad (3)$$

Here ϕ is porosity, C_i is the concentration of i, t is time, D_i is the diffusion/dispersion coefficient, u is the flow velocity, N_r is the total number of kinetic aqueous reactions that involve species i, ν_{ir} is the stoichiometric coefficient of the species i associated with the reaction r, R_r is the rate of aqueous reaction r, N_m is the total number of mineral reactions that involve species i, ν_{im} is the stoichiometric coefficient of the species i associated with the reaction m, and R_m is the rate of mineral reaction m. Eq. (3) implies that the mass change rate of species i depends on several processes: the diffusion/dispersion processes that are accounted for by the first term of the right hand side of the equation, the advection process that is taken into account by the second term of the right hand side, and reaction processes, taken into account by the last two terms of the equation. The last two terms are the summation of several terms, the length and form of which depend on the number and type of kinetic reactions that species i is involved in.

The reaction network includes both the kinetically controlled reactions such as the three major bioreduction reactions and mineral dissolution and precipitation reactions, as shown in Fig. 1. The mineral phases included calcite, magnesite, siderite, FeS(am), and Fe(OH)$_3$. The hydrous iron oxide can react with S($-$II) generated from sulfate reduction to produce elemental sulfur (Yao and Millero, 1996). The reaction network also includes fast reactions that are considered at equilibrium, including ion exchange and aqueous complexation reactions, all of which are shown in Tables 4 and 5. The equations for the three bioreduction reactions were obtained using the methodology introduced by Rittmann and McCarty (2001), taking into account the bacterial energetics. The form of the rate laws of the kinetically controlled reactions depend on the type of reactions. For microbially-mediated reactions, we use the following Monod rate law (Monod, 1949; Rittmann and McCarty, 2001) that explicitly takes into account the effect of microbial growth and the competition between different electron acceptors:

$$r_s = -k_{max} X_S(x,t) \frac{C_S}{K_{M,S} + C_S} \frac{C_{TEA}}{K_{M,TEA} + C_{TEA}} \frac{K_I}{K_I + C_I}. \quad (4)$$

Here the reaction rate r_s of the electron donor S depends on the maximum utilization rate k_{max} (mol/L/s/cells), the space and time dependent concentration of the bacteria, X_S (cells), that utilize the electron donor, the concentration of the electron donor (C_S) and the terminal electron acceptor (C_{TEA}) through the dual Monod terms with their respective

Table 5
Instantaneous aqueous speciation reactions included in the model and their equilibrium constants.

Instantaneous aqueous speciation reactions	$\log K_{eq}$
$H_2O \rightleftharpoons H^+ + OH^-$	-14.0
$HCO_3^- + H^+ \rightleftharpoons CO_2(aq) + H_2O$	6.34
$CO_3^{2-} + 2H^+ \rightleftharpoons CO_2(aq) + H_2O$	16.7
$FeOH^+ + H^+ \rightleftharpoons Fe^{2+} + H_2O$	9.50
$Fe(OH)_2(aq) + 2H^+ \rightleftharpoons Fe^{2+} + 2H_2O$	20.6
$Fe(OH)^-{}_3 + 3H^+ \rightleftharpoons Fe^{2+} + 3H_2O$	31.0
$FeOH^{2+} + H^+ \rightleftharpoons Fe^{3+} + H_2O$	2.19
$FeCl^+ \rightleftharpoons Fe^{2+} + Cl^-$	0.165
$FeCl^{2+} \rightleftharpoons Fe^{3+} + Cl^-$	0.815
$Fe(OH)_2^+ + 2H^+ \rightleftharpoons Fe^{3+} + 2H_2O$	5.67
$Fe(OH)_3(aq) + 3H^+ \rightleftharpoons Fe^{3+} + 3H_2O$	12.0
$FeS(aq) + 2H^+ \rightleftharpoons Fe^{2+} + H_2S(aq)$	9.20
$FeCO_3(aq) + 2H^+ \rightleftharpoons Fe^{2+} + CO_2(aq) + H_2O$	11.9
$Fe(CH_3COO)_2(aq) \rightleftharpoons Fe^{2+} + 2CH_3COO^-$	-2.48
$FeCH_3COO^+ \rightleftharpoons Fe^{2+} + CH_3COO^-$	-1.29
$CaOH^+ + H^+ \rightleftharpoons Ca^{2+} + H_2O$	12.9
$CaCO_3(aq) + 2H^+ \rightleftharpoons Ca^{2+} + H_2O + CO_2(aq)$	13.4
$CaSO_4(aq) \rightleftharpoons Ca^{2+} + SO_4^{2-}$	-2.1
$CaCl^+ \rightleftharpoons Ca^{2+} + Cl^-$	0.7
$CaHCO_3^+ + H^+ \rightleftharpoons Ca^{2+} + H_2O + CO_2(aq)$	5.3
$Ca(CH_3COO)_2(aq) \rightleftharpoons Ca^{2+} + 2CH_3COO^-$	-2.13
$CaCH_3COO^+ \rightleftharpoons Ca^{2+} + CH_3COO^-$	-0.928
$MgCO_3(aq) + 2H^+ \rightleftharpoons Mg^{2+} + H_2O + CO_2(aq)$	13.7
$MgCl^+ \rightleftharpoons Mg^{2+} + Cl^-$	0.139
$MgSO_4(aq) \rightleftharpoons Mg^{2+} + SO_4^{2-}$	-2.41
$CH_3COOH(aq) \rightleftharpoons H^+ + CH_3COO^-$	-4.75
$HS^- + H^+ \rightleftharpoons H_2S(aq)$	6.98
$S^{2-} + 2H^+ \rightleftharpoons H_2S(aq)$	19.9
$NH_3(aq) + H^+ \rightleftharpoons NH_4^+$	9.24
$UO_2CO_3(aq) + 2H^+ \rightleftharpoons UO_2^{2+} + H_2O + CO_2(aq)$	7.00
$UO_2SO_4(aq) \rightleftharpoons UO_2^{2+} + SO_4^{2-}$	-3.07
$CaUO_2(CO_3)_3^{2-} + 6H^+ \rightleftharpoons Ca^{2+} + UO_2^{2+} + 3H_2O + 3CO_2(aq)$	22.8
$UO_2(CO_3)_2^{2-} + 4H^+ \rightleftharpoons UO_2^{2+} + 2H_2O + 2CO_2(aq)$	16.4
$UO_2(CO_3)_3^{4-} + 6H^+ \rightleftharpoons UO_2^{2+} + 3H_2O + 3CO_2(aq)$	28.5

half-saturation constants $K_{M,S}$ and $K_{M,TEA}$ (mol/L), as well as the inhibition term, with K_I being the inhibition constant (mol/L) and C_I being the concentration of the inhibiting substance I (mol/L).

The inhibition term takes into account the competition between different electron acceptors. For example, bioreduction reactions that occur under anaerobic conditions typically use nitrate as the electron acceptor first (when available), then Fe(III), U(VI), and SO$_4^{2-}$, the order of which is determined by the decreasing amount of energy that bacteria can obtain by utilizing the electron acceptors. For the Rifle site, because of the negligible concentrations of dissolved oxygen and nitrate, no inhibition term for iron and uranium reduction is used. Sulfate reduction is inhibited by the amount of Fe(III) locally. As such, sulfate reduction occurs after the bioavailable Fe(III) has been consumed to a significant extent. As listed in Table 4, all reaction-related parameters in Eq. (4) were obtained from literature except for the k_{max} values.

In this work, we explicitly model the growth of two microbial communities, the FeRB and SRB, according to reactions 1 and 2 (Table 4) at the rate specified by Eq. (4). It is assumed that the bacteria are immobile because the majority of the cells tend to attach to the solid phase, either in the form of biofilms or separate microbial colonies (Griebler et al., 2002; Lloyd, 2003; Rittmann and McCarty, 2001). The microbial populations evolve with time and space, depending

on the concentration of electron acceptor, donor, inhibitors, and the amount of each microbial population at specific time and location, as indicated in Eq. (4). The yield coefficients for the generation of the microbial populations were taken as 0.018 and 0.003 g biomass (dry weight)/mmol acetate for FeRB and SRB, respectively, as can be calculated from stoichiometric coefficients of the reactions 1 and 2. These numbers are equivalent to yield coefficients of 0.16 and 0.03 mol biomass/mol substrate, respectively, as defined in VanBriesen (2002). The yield coefficient for FeRB is in the typical range of those reported in literature specifically for *Geobacterae* (Cord-Ruwisch et al., 1998; Esteve-Núñez et al., 2005; Mahadevan et al., 2006; Rutgers et al., 1989), because the yield coefficients of a specific bacterium can vary within an order of magnitude, depending on their growth condition and growth phase (Rittmann and McCarty, 2001; Rutgers et al., 1989). The molar volume of the biomass was assumed to be 336.0 cm^3/mol, a number in the middle of the range of those reported in the literature (Loferer-Krossbacher et al., 1998). The model does not include the death of bacteria, because dead cells still have volume and need to be counted in the calculation of pore volume being occupied by biomass.

The rates of mineral dissolution and precipitation are assumed to follow the rate law derived from Transition State Theory (TST) (Lasaga, 1998), with a typical reaction rate constant and a term indicating the saturation state of the reaction. For example, for calcite dissolution and precipitation, we have the following rate law:

$$R = Ak\left(1 - \frac{IAP}{K_{eq}}\right). \qquad (5)$$

Here k is the reaction rate constant, IAP is the ion activity product defined as $a_{ca^{2+}}a_{CO_3^{2-}}$, K_{eq} is the equilibrium constant for the reaction, and A is the reactive surface area. Table 4 lists important reactions, as well as their kinetic and thermodynamic parameters, including values of k and K_{eq}.

The reactive transport simulations were carried out within a 24 meter by 20 meter domain, with 7857 (97 × 81) grids and a fixed resolution of 24.7 cm. The steady-state flow field was calculated using the hydraulic conductivity field determined from the inverse methods described above, a constant pressure difference between the upstream and downstream boundary (y direction), and a no-flow boundary condition in the direction parallel to the main flow (x direction). The dispersivity was chosen to be 0.40 m to best fit the tracer field data, which is also a typical value of dispersivity for a spatial scale of tens of centimeters (Gelhar et al., 1992). The porosity was fixed at 0.27, the mean porosity of the system, to be consistent with the assumption for the inverse modeling. The initial and boundary conditions for the aqueous species were chosen to be the measured background composition of the Rifle site, as listed in Table 1. Initially both FeRB and SRB are considered to exist ubiquitously, occupying 10^{-4} volume percentage of the solid phase, corresponding to a cell density between 3×10^5 to 9×10^6 cells/mL of the sediment (Dr. Aaron Peacock; personal communication), within the typical cell density range of 10^4 to 10^7 cells/mL of the sediment (Pallud and Van Cappellen, 2006).

The field experiments were carried out for two successive years. Accordingly, the simulations were carried out with the initial conditions of the 2003 experiment set to be the final state of the 2002 experiment. By fitting to the breakthrough curves of various aqueous species, including acetate, sulfate, uranium, and Br$^-$, we obtain a set of parameters that best describe the dynamics of the biogeochemical system. Based on the constraints by the field data, the amount of mineral precipitates and biomass at different times and locations were then estimated.

4. Results

4.1. Hydraulic conductivity field and Fe(III) content field

Fig. 2A shows a single realization of hydraulic conductivity field obtained through inversion of the Br$^-$ tracer data (see Section 3.1). Fig. 2B shows the realization of bioavailable iron content field corresponding to Fig. 2A, obtained using the approach described in Section 3.2. The bioavailable Fe(III) content is shown as a volume fraction of the pore space, which is the ratio of the volume of iron (hydro)oxide over the volume of the pore space. Values of hydraulic conductivity vary significantly in space, spanning more than 4 orders of magnitude due to the heterogeneous nature of the Rifle sediments. Comparison between Fig. 2A and B shows that wherever the hydraulic conductivity value is high, the Fe(III) content is low, demonstrating the negative correlation between the two variables that was assumed based on the results in Table 4.

4.2. Fit to the field data

In this section we compare the modeling output with the 2002 breakthrough curves of acetate and sulfate from the 15 monitoring wells. Although not shown here, the modeling output also fits the 2003 breakthrough curves of aqueous species well. The fit was obtained by adjusting kinetic parameters using trial and error. The simulations were not very sensitive to the initial amounts of biomass; with the same set of kinetics parameters, even changes of initial biomass by orders of magnitude do not affect the simulation results much. As can be seen from Figs. 3 and 4, the modeling output accurately matches the time when the pulse of acetate arrives, indicating that the model has adequately captured the dynamics of the system. The good match between field data and modeling output provides strong constraints for the estimation of mineral precipitates and biomass.

4.3. Reactive transport processes

In this section the concentration profiles of several key aqueous species at various stages of the field experiments will be shown to illustrate the coupling between the transport and biogeochemical processes. During the experiment, bromide and acetate were mixed with native groundwater and were injected into the subsurface. Bromide is a non-reactive tracer while acetate reacts with various electron acceptors at the site, including Fe(III), U(VI), and sulfate. The difference between the concentration profiles of bromide and acetate provides information on where and to what extent reactions
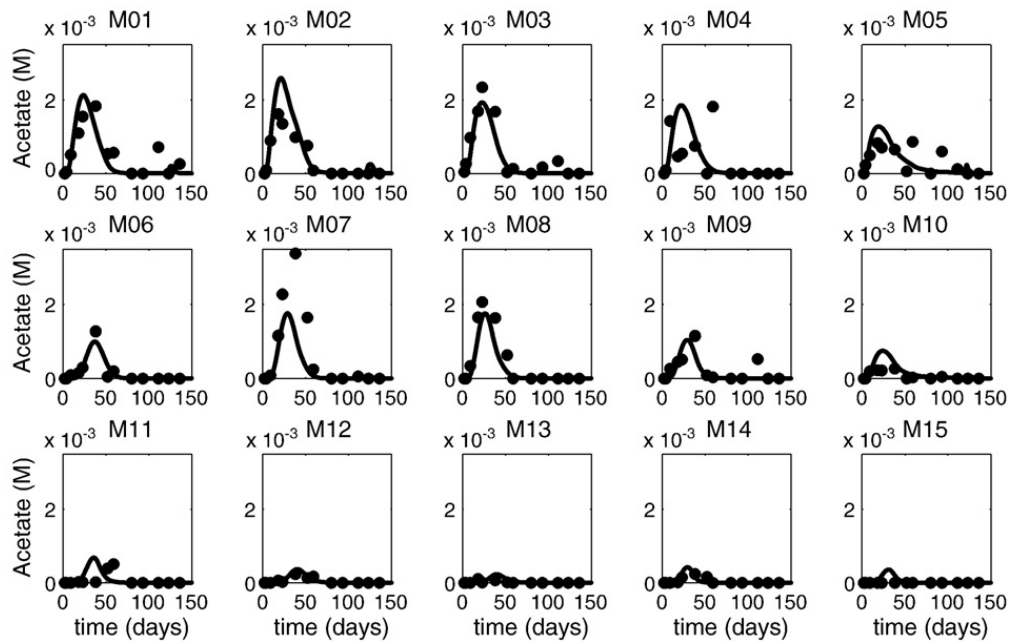
Fig. 3. Comparison between acetate breakthrough curves in 2002 (dots) with the model output (lines). Acetate concentrations are show in M (mol/L).

have occurred. Fig. 5 shows the concentration profiles of bromide, acetate, and sulfate at day 25 in 2002, at the end of 2002 experiment, and at the end of 2003 experiment. The spatial distributions of bromide are quite heterogeneous. Close to the injection wells, injected chemicals accumulated in regions of low hydraulic conductivity where the flow is relatively slow. In down-gradient regions, bromide and acetate tend to transport through areas of high hydraulic conductivity while bypassing those of low hydraulic conductivity. The shape of the Br^- plumes is solely determined by the spatial distribution of the hydraulic conductivity.

In contrast, the shape of the acetate plume is a result of interactions between transport and biogeochemical reactions. Its concentration profile is similar to that of bromide at day 25 in 2002 (Fig. 5A and D), because in the early stages of the experiment when iron reduction dominates, there is not much consumption of acetate due to the relatively low abundance of bioavailable Fe(III) in the major flow paths. Still, we see some differences between the plumes, especially in regions where bioavailable Fe(III) is relatively abundant (as seen in Fig. 2B). At the end of the 2002 experiment (Fig. 5B and E), the concentration profiles of bromide and acetate show significant
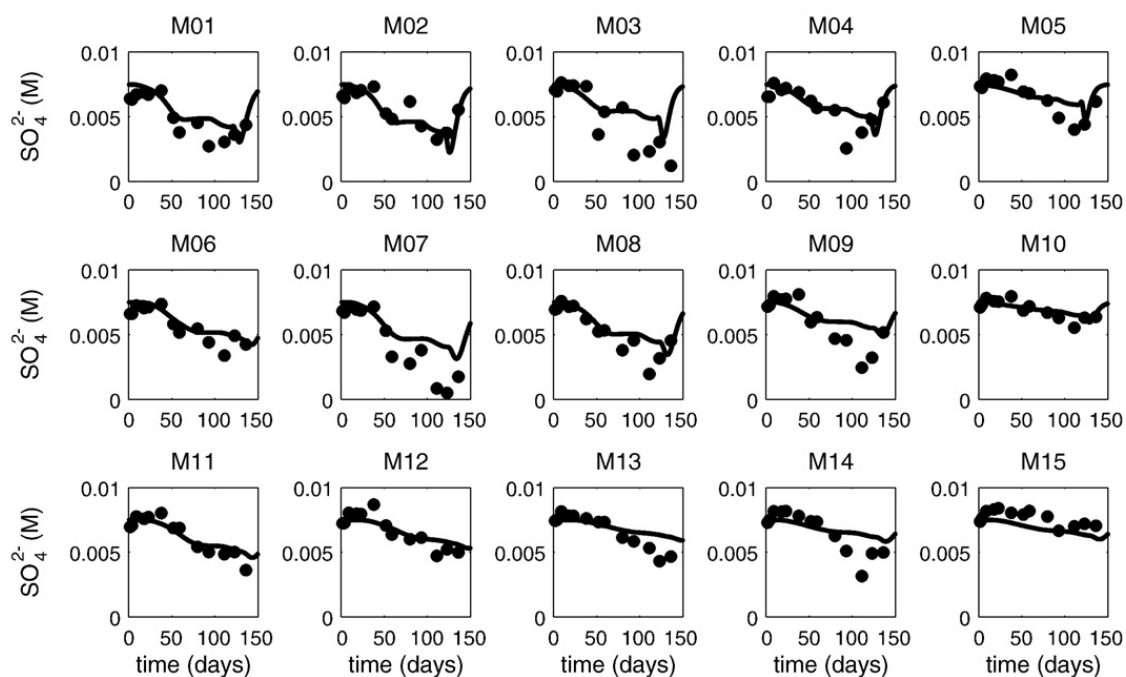

Fig. 4. Comparison between sulfate breakthrough curves from the fifteen monitoring wells in 2002 (dots) with the model output (lines).
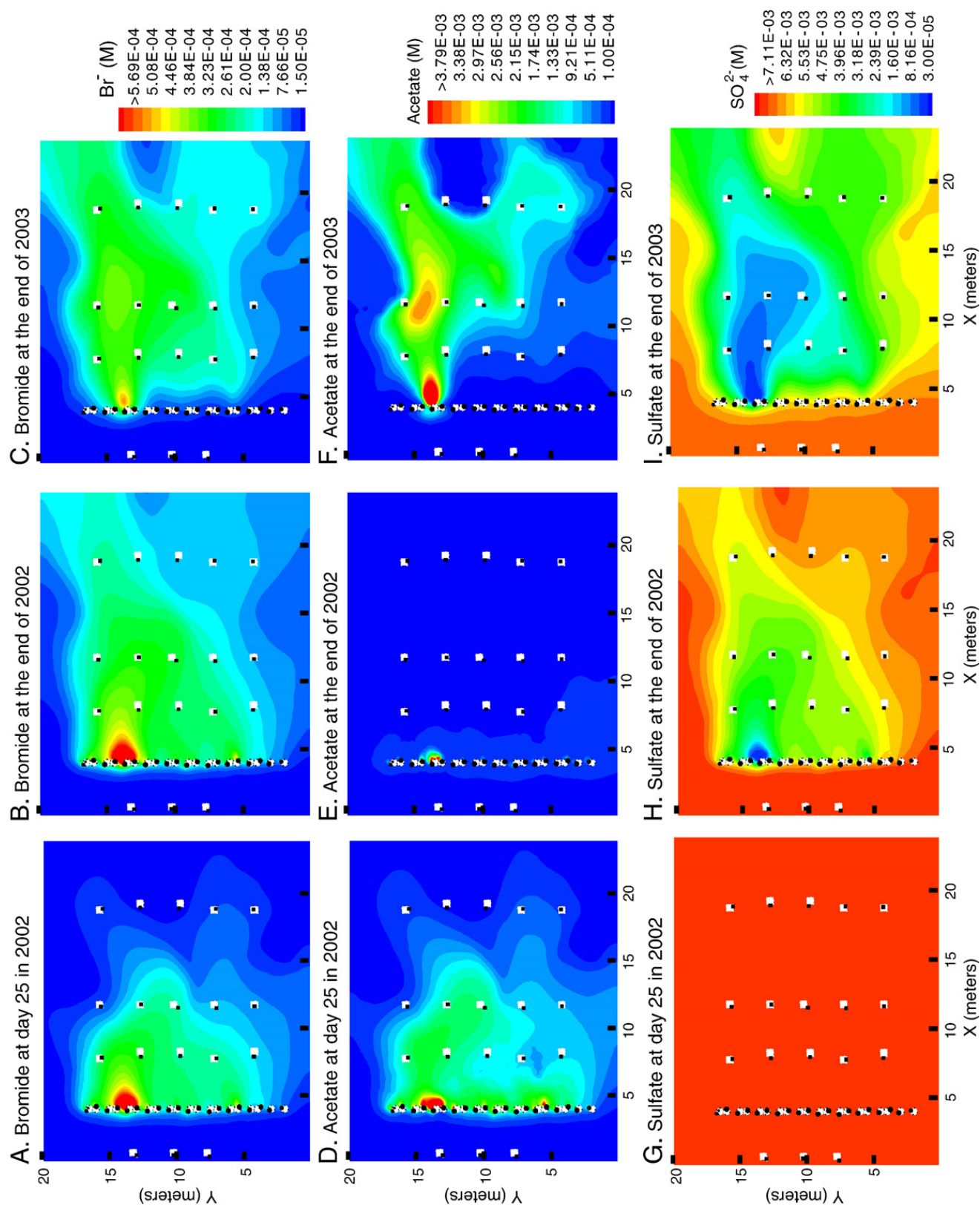
Fig. 5. Comparison of Br⁻, acetate, and sulfate concentration profiles at day 25 in 2002, at the end of 2002 experiment, and at the end of 2003 experiment.

differences. A large plume of bromide extends from the injection gallery to areas well beyond the third row of monitoring wells, with a shape consistent with the spatial variation of the hydraulic conductivity. In contrast, acetate only showed up in a tiny region of the injection gallery with low hydraulic conductivity. This huge difference is caused by the reactive nature of acetate. At later times after bioavailable Fe(III) was depleted close to the injection wells, sulfate reduction dominated. Because sulfate exists in the groundwater with high concentrations (~7–9 mM) and is continuously supplied from the up-gradient groundwater, acetate is quickly used up by sulfate reducers in regions close to the injection wells, leaving no acetate to transport to down-gradient regions. Note that in the 2003 experiment (Fig. 5F), however, the situation is different. The 2003 experiments injected the same amount of bromide as in 2002, while tripling the amount of injected acetate, targeting a tripled concentration of acetate in the groundwater. As a result, the sulfate close to the injection wells was not enough to deplete acetate, which allowed some of the acetate to transport to and react in down-gradient regions.

The concentration profiles of sulfate show similar dynamics. Within the first 25 days of the 2002 experiment (Fig. 5G), before bioavailable Fe(III) was depleted, sulfate reduction did not occur and sulfate existed everywhere with its background concentration of approximately 7.5 mM. At the end of 2002 (Fig. 5H), however, low concentrations occur close to the injection wells. The lowest concentration of sulfate occurred exactly at the same location as the maximum concentration of acetate in Fig. 5E. In down-gradient regions and at the plume fringe, sulfate concentration started to "recover," returning to the concentration in the background level. At the end of 2003 experiment (Fig. 5I), with much higher concentrations of acetate in the groundwater, there were much larger regions of sulfate depletion than at the end of 2002. The regions of sulfate depletion coincide with those of highest Br^- concentrations, indicating that acetate tends to be transported through the same high hydraulic conductivity regions as bromide, therefore consuming sulfate in these regions. This is consistent with findings from another study for the Rifle site that there is a high correlation between bromide and sulfate accumulated mass distributions in both 2002 and 2003 (Englert et al., 2009).

4.4. Evolution of minerals and biomass

In this section we aim to understand the spatial patterns of mineral precipitates and biomass accumulation. Fig. 6 shows the time evolution of the spatial distribution of bioavailable Fe(III). As expected from the profile of acetate, the depletion of Fe(III) started in regions close to the injection wells, and then extended to down-gradient regions. Comparison between Figs. 6 and 5D–F indicates that Fe(III) is consumed only in regions where both acetate and Fe(III) coexist. Because acetate concentrations close to the injection wells were high, bioavailable Fe(III) was completely depleted in these regions. In down-gradient regions, however, acetate is only transported through regions of high conductivity and depleted bioreducible Fe(III). In some regions where hydraulic conductivity is low, bioavailable Fe(III) persists even after the 2003 experiment.

Fig. 7 shows the spatial distributions of the iron reducers and sulfate reducers at day 25 in 2002, at the end of 2002 experiment, and at the end of 2003 experiment. The two microbial populations show very different temporal and spatial patterns of growth. The iron reducers grew within the first 25 days of acetate injection, starting from the vicinity of the injection wells and progressively expanding to the down-gradient regions containing bioavailable iron and acetate. At the end of 2003, the iron reducers have grown in most areas containing bioavailable iron, except in relatively small regions that acetate has totally bypassed in both experiments. As a result, the spatial distribution of FeRB resembles that of the bioavailable iron content and is very much shaped by the geochemical heterogeneity of the domain.

In contrast, sulfate reducers did not start to grow until after 25 days when the bioavailable iron in the vicinity of the injection wells has been depleted. The sulfate reducers started to grow after 25 days, but their growth focused only in regions close to the injection wells. This is again because sulfate exists in the groundwater in high concentrations and is continuously supplied from the up-gradient groundwater. After the onset of sulfate reduction in the vicinity of the injection wells, the injected acetate was quickly consumed by sulfate reducing bacteria and cannot be transported to down-gradient regions. This is why the accumulation of sulfate reducers is more than an order of magnitude larger than that of iron reducers in the vicinity of the injection wells. Although acetate did reach down-gradient regions in 2003, it reacted primarily with Fe(III) in these regions, significantly adding to the amount of iron reducers while not increasing the amount of sulfate reducers in these regions. As a result, the sulfate reducers grew mostly in the vicinity of the injection wells and are not strongly affected by either the physical or geochemical heterogeneities of the domain. At the end of 2003, the SRB reached a maximum of volume fraction of 2.9% of the pore space, while the maximum of FeRB was only 0.16 vol.% fraction of the pore space.

Fig. 8 shows the spatial distribution of several important precipitates as well as that of the total amount of precipitates and biomass at the end of 2003. The mineral precipitates include calcite, FeS(am), magnesite, siderite, uraninite, and elemental sulfur, although not all of them are shown. It is obvious that calcite is the dominant precipitate. This is because the carbonate species are the products of all three bioreduction reactions and accumulate wherever bioreduction reactions occurred. The carbonate species can quickly react with Ca^{2+} or Mg^{2+} in the groundwater to form calcite or magnesite, respectively. However, the higher solubility of magnesite results in a significantly lower amount of it precipitated than calcite. Not shown in the figure is the precipitated siderite, which occupies approximately 10^{-5} of the pore space at maximum according to the simulations.

The precipitate FeS(am) (Fig. 8C) is a reaction product of the Fe(II) generated by iron bioreduction and S(−II) generated by sulfate bioreduction, while elemental sulfur is a reaction product of the abiotic reduction of Fe(III) by S(−II). $UO_2(s)$ is the reaction product of U(VI) bioreduction. All these precipitates form in amounts at least an order of magnitude lower than calcite. In all cases, the maximum precipitation occurs in the vicinity of the injection wells. Uraninite also
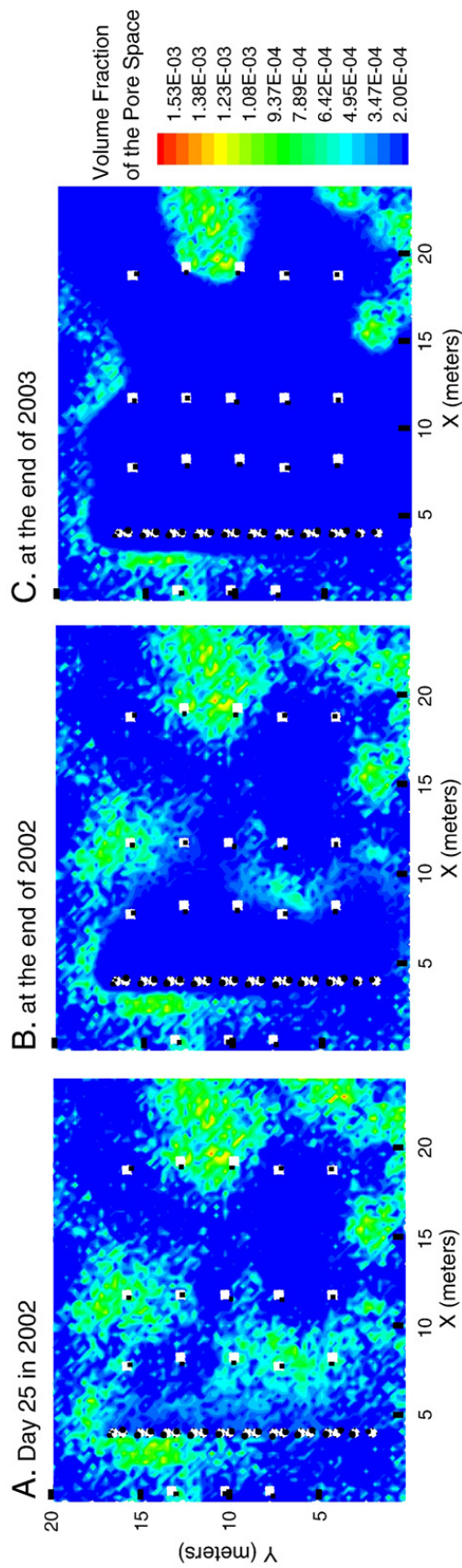
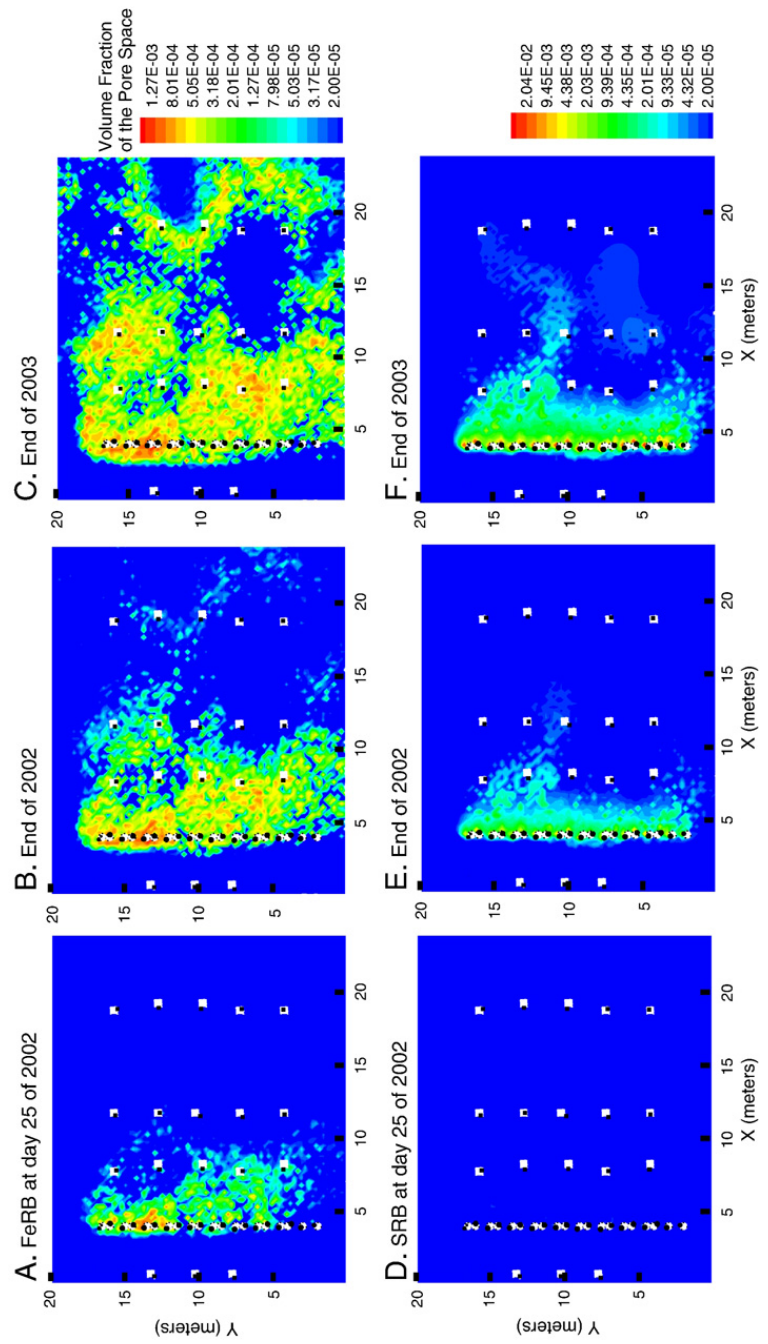**Fig. 6.** Evolution of the bioavailable Fe(III) field.

Fig. 7. Spatial distributions of FeRB and SRB at day 25 in 2002, at the end of 2002 experiment, and at the end of 2003 experiment.
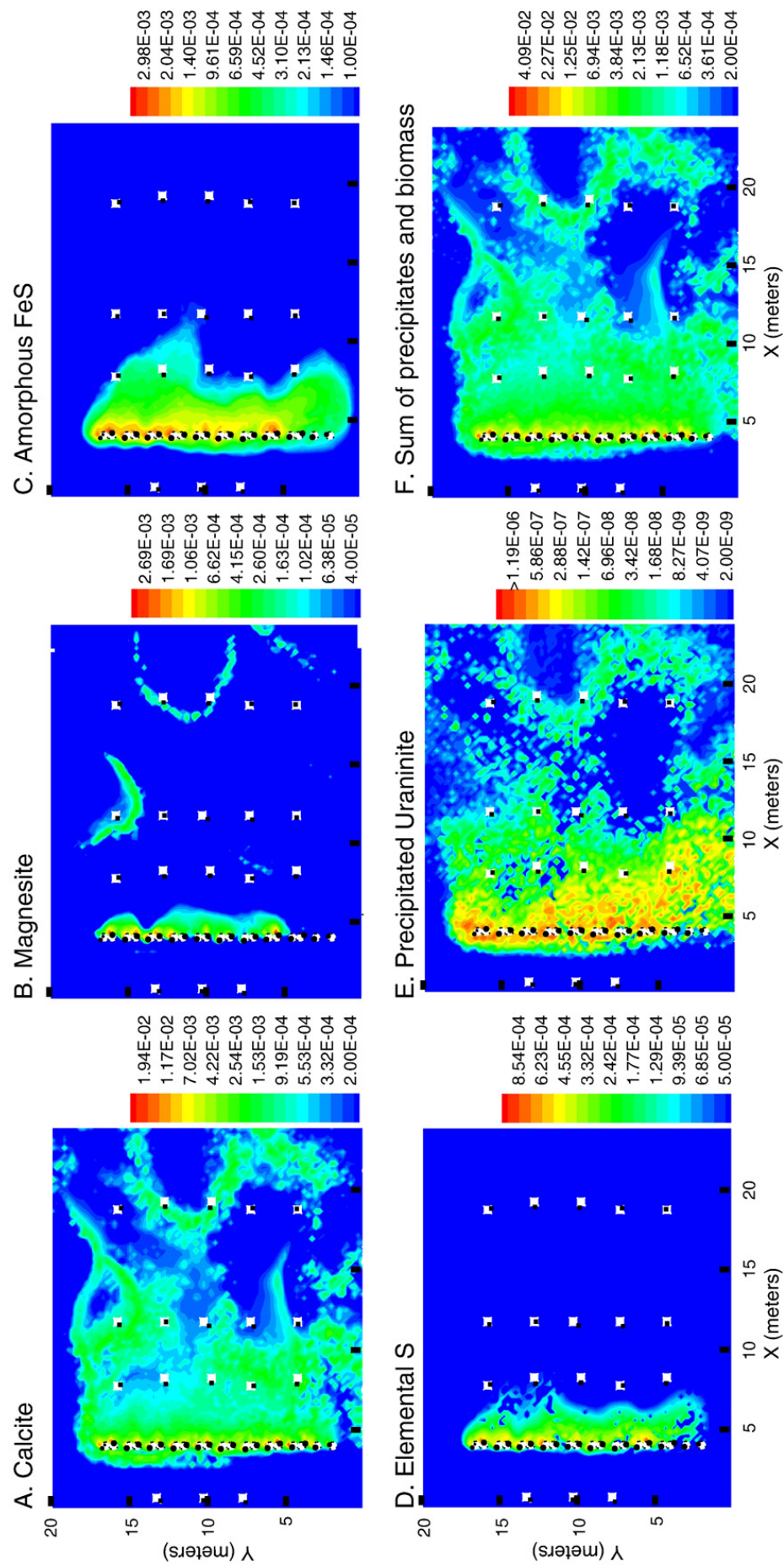
Fig. 8. Spatial distributions of calcite, magnesite, FeS(am), elemental sulfur, $UO_2(s)$, and the sum of all precipitates and biomass at the end of 2003 experiment. The values are the volume fractions of the pore space that different precipitates and/or biomass occupy.

precipitates in down-gradient regions where FeRB exist, however, at an amount 2 to 3 orders of magnitude lower than that in the vicinity of the injection wells.

Fig. 9 shows the evolution of the spatial distribution of mineral precipitates at different times. The spatial distributions exhibit quite different patterns from that of both FeRB and SRB. Precipitation reactions occur wherever the products of microbially-mediated reactions reached saturation with respect to one or more of the mineral phases, and thus the spatial distribution of precipitates reflects where reactions occur, whether it is iron reduction, sulfate reduction, or uranium reduction. As a result, the spatial distributions of mineral precipitates appear like the summation of the patterns of iron reducers and sulfate reducers. At day 25, the spatial distribution of the minerals looks very similar to that of the iron reducers, while at later times after the onset of sulfate reduction, the patterns appear similar to that of the sulfate reducers in regions close to the injection wells and that of the iron reducers in down-gradient areas. The maximum occurs close to the injection wells, reaching as much as 2.5% by volume of the pore space. As a result the total amount of biomass and mineral precipitates reaches as high as 5.4% by volume of the pore space.

4.5. Comparison between 1D homogeneous and 2D heterogeneous systems

In this section we compare the spatial profiles and reaction rates from the current 2D simulation to those from the 1D simulation in our previous work (Li et al., 2009). The purpose of our previous work was to develop a reaction network and a reactive transport model based on column experiments and make predictions in the field using the same reaction network. As is the case in this study, the 1D prediction of biomass and mineral precipitates was obtained using reactive transport modeling constrained by the field aqueous geochemistry data from various monitoring wells. However, the 1D simulations were carried out based on the assumption that the field experiment domain is homogeneous, with spatially constant hydraulic conductivity and Fe(III) content. Although these values are the same as the mean values for the 2D system, the 1D system ignores the effects of the heterogeneities. As such, comparison between the two provides insights into the effects of heterogeneities on the accumulated biomass and reaction rates.

Fig. 10 shows the 1D spatial profiles of FeRB, SRB, and precipitated uraninite at the end of 2003 experiment for the two systems. For comparison the 2D spatial profiles shown in Figs. 7C, F, and 8E were averaged over the direction transverse to the principal groundwater flow direction (y direction), resulting in a 1D spatial profile in the direction of main groundwater flow that can be compared to the 1D prediction. For FeRB, as can be observed from Fig. 10A, the spatial profiles from the two systems are quite different. At the end of 2003, the 1D system predicts a maximum growth of FeRB in all regions down-gradient to the injection wells, while the 2D Y (transverse)-averaged profile shows spatially variable accumulation of FeRB in downstream regions with the averaged maximum does occur close to the injection wells. The FeRB accumulation in the downstream regions is in general smaller than the maximum accumulation predicted by the 1D system,

although it fluctuates instead of monotonically decreases with increasing distance from the injection wells. Such fluctuation is caused by the heterogeneous distribution of hydraulic conductivity that leads to preferred flow paths through regions of high hydraulic conductivity but low iron content. These preferred flow paths bypass areas with high iron content that do not experience significant FeRB growth, especially in regions far away from the injection wells. As such, the spatial variation is a result of the effects of physical and geochemical heterogeneities, especially the negative coupling between the two, on the FeRB accumulation.

In contrast, the spatial profiles of SRB from the 1D and 2D systems are very similar, to the extent that they almost fall onto each other. Consistent with findings presented in previous subsections and in previous work (Li et al., 2009), a sharp maximum accumulation of SRB occurs close to the injection wells, and quickly drops to zero in downstream regions in both the 1D and 2D systems. This indicates that the average accumulation of sulfate reducers is not strongly affected by the heterogeneities of the system — the growth of sulfate reducers always focuses on regions close to the injection wells. However, the fact that the averaged maximum for the 2D system is the same as the 1D system does not guarantee that the local maximum from the 2D system is the same. The maximum SRB accumulation predicted by the 1D system is approximately 0.5 vol.% of the pore space (Li et al., 2009), about 6 times lower than the 2.9 vol.% of the pore space predicted from the 2D heterogeneous cases. Because pore clogging processes occur locally and depend strongly on local maximums instead of averaged values, the heterogeneities of the system can still have a large impact on such processes.

With the close association of uranium reduction with FeRB, one would expect that the 2D Y-averaged spatial distribution of uraninite looks very similar to that of FeRB. However, 2D Y-averaged spatial distribution of precipitated uraninite actually looks quite different from that of FeRB and is similar to that from the 1D homogeneous system. Such similarity may be due to the fact that uranium itself shares some similar features with sulfate in that it is ubiquitously distributed in the groundwater and has a continuous supply from the up-gradient. As a result, with the grown FeRB and accessible acetate, regions close to the injection wells served as a reaction barrier that continuously reduced uranium and precipitated uraninite. It is in this region that the uraninite concentration reaches its maximum. In regions down-gradient, although there is precipitated uraninite, the amount is orders of magnitude smaller, as shown in Fig. 8E. This may imply that geochemical heterogeneities close to the injection wells are much more important to determine the uranium bioremediation efficacy than that in down-gradient regions.

The strong impact of heterogeneities on the Fe(III) reduction process also implies a strong control over the rate and the extent to which Fe(III) was depleted in the experiments. Fig. 11A shows the time evolution of the averaged Fe(III) content in 2002, averaged over the whole experimental domain for both systems. The 1D homogenous system shows a much higher rate and extent of Fe(III) depletion than the 2D heterogeneous case. In the rapidly decreasing period (from day 10 to day 75), the 1D rate is 0.013 μmol/g/day, twice of the 2D rate of 0.0067 μmol/g/day. At the end of 2002, the total amount of Fe(III) that has been reduced in the 1D system is
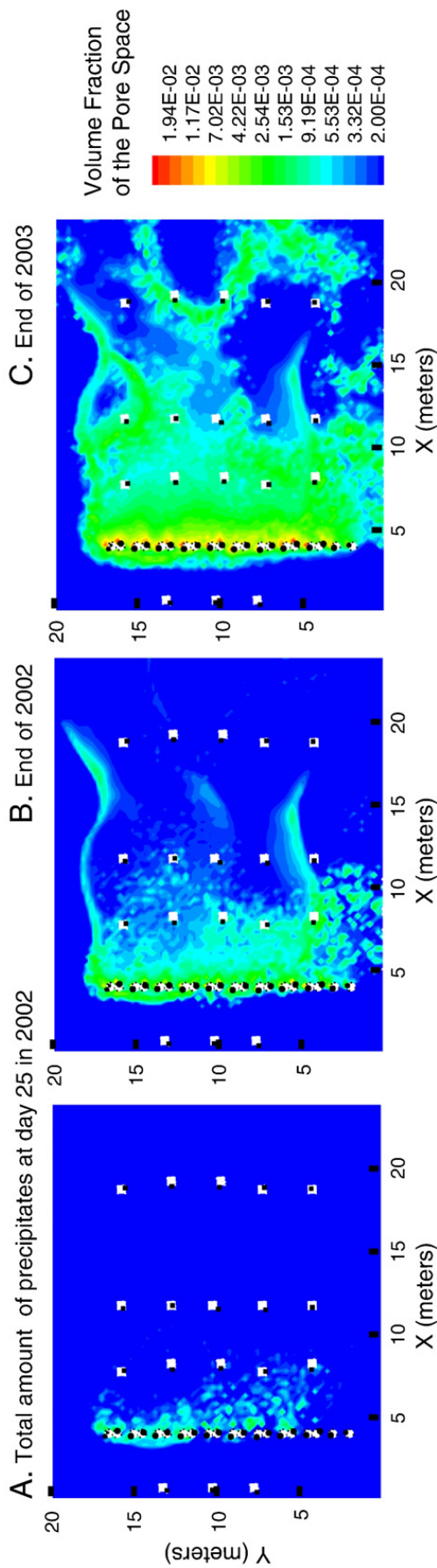
Fig. 9. Spatial distributions of total amount of mineral precipitates in day 25 in 2002 experiment, at the end of 2002 experiment, and at the end of 2003 experiment.
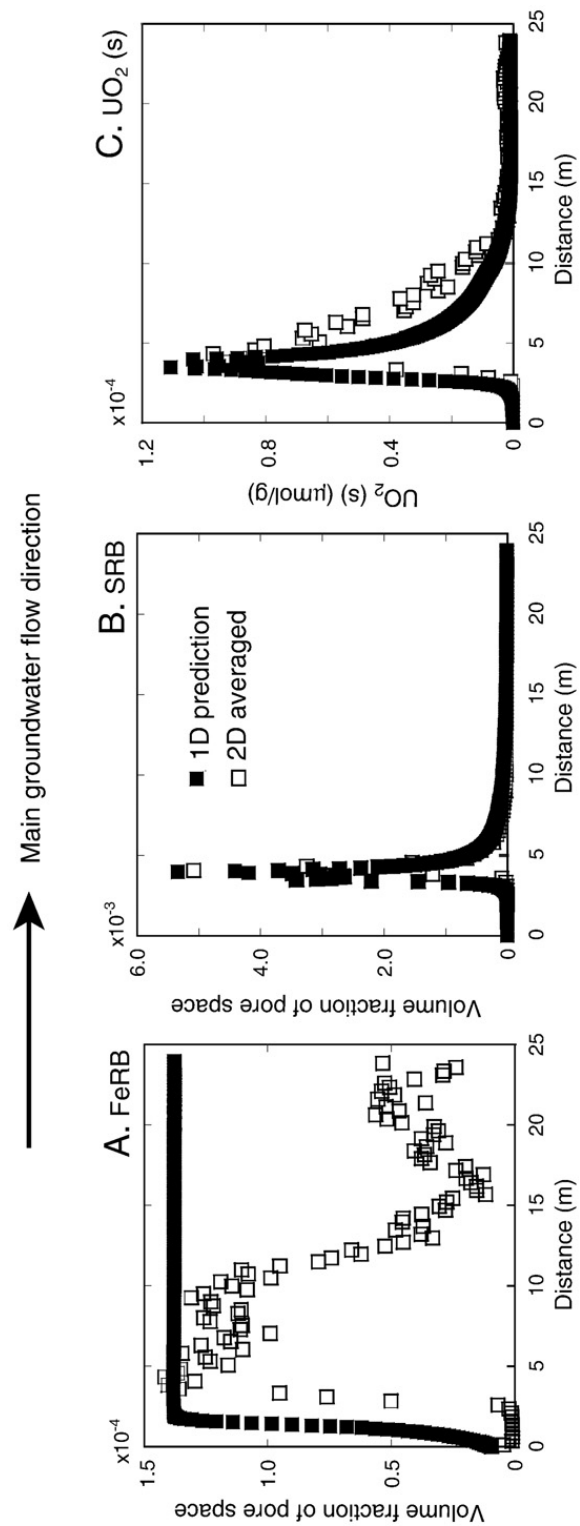

Fig. 10. Profiles of FeRB, SRB, and UO$_2$(s) at the end of 2003 experiment in the groundwater flow direction. Comparison is made for prediction from a 1D simulation (Li et al., 2009) and 2D simulation (this study, averaged over the direction perpendicular to the main groundwater flow direction).
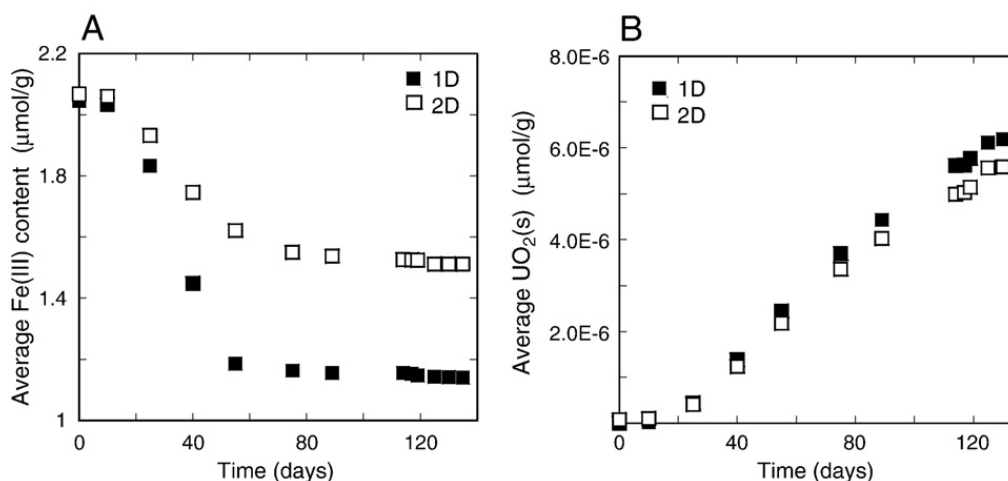
Fig. 11. Time evolution of the bioavailable Fe(III) content (A) and $UO_2(s)$ (B) in 2002, averaged over the whole domain for both 1D and 2D systems.

about two times larger than that reduced in the 2D hetero-geneous system. As such, ignoring the physical and geochemical heterogeneities of the system can lead to an overestimation of FeRB accumulation, as well as the rate and the extent of Fe(III) depletion.

The predicted rates of uraninite precipitation are actually very similar for the two systems, as shown in Fig. 11B. This is expected given that 2D Y-averaged spatial profile looks very similar to that of 1D prediction. Notice that this is an observation for one realization of the hydraulic conductivity field and iron content field. With a slightly different field, perhaps with different characteristics of iron content close to the injection wells, the overall amount of uraninite precipitation might be different.

4.6. Discussion

The temporal and spatial evolution of the aqueous species, the mineral phases, and the microbial community show that after acetate injection began, bioavailable Fe(III) was depleted initially close to the injection wells, thus triggering the onset of sulfate reduction. The vigor with which sulfate reduction occurred close to the injection wells in the 2002 experiment results in the depletion of acetate in this region, thus preventing it from migrating downstream in significant quantities for the remainder of the 2002 experiment. In the 2003 experiment in which the injection concentration of acetate was tripled (thus exceeding the supply of sulfate in the groundwater), some of acetate was transported to down-gradient regions and further reduced the Fe(III) and U(VI) in these locations. These findings are consistent with other observations from the Rifle site (Anderson et al., 2003; Li et al., 2009; Vrionis et al., 2005). For example, by analyzing the geochemical conditions and microbial gene expressions from different monitoring wells, Vrionis et al. (2005) found that close to the injection wells, microbially reducible Fe(III) was highly depleted, acid volatile sulfide was observed, sulfate concentrations were low, and the sulfate-reducing bacteria predominated. Through gene-based and lipid-based microbial community analysis, Anderson et al. (2003) also found that the composition of the microbial community changed over time during the experiment, with *Geobacter* (FeRB) dominating

in early times and being replaced by SRB as the dominant community at later times. They also observed that the complete consumption of acetate under sulfate-reducing conditions near the injection wells prevented further metal reduction in down-gradient regions.

The temporal and spatial evolution of mineral precipitates and biomass are affected by physical and geochemical heterogeneities to a different extent, depending on the type of reactions that they originated from. The reaction products of iron reduction develop in both the vicinity of the injection wells and in down-gradient regions, and their spatial distributions are strongly shaped by both pre-existing physical and geochemical heterogeneities. The reaction products of sulfate reduction, however, occur close to the injection wells for the most part and are not influenced as strongly by physical and geochemical heterogeneities.

This work implies that the extent to which physical and geochemical heterogeneities control the spatial distributions of biomass and mineral precipitates depends on the general geochemical conditions at the site. The relatively high concentrations of sulfate in the groundwater at the Rifle site exert a strong control on the extent to which subsurface heterogeneities affect biogeochemical processes at the site. As such, the ratio of the electron donor (acetate in this case) to the electron acceptors (microbially reducible Fe(III) phases or sulfate) on an electron-equivalent basis can be a key parameter here. If sulfate exists at much lower concentrations and does not deplete acetate upon injection, or, if the Rifle sediment is richer in the amount of microbially reducible Fe(III), physical heterogeneity would play a much more significant role in shaping the spatial patterns of the reaction products of sulfate reduction because it can play a larger role in determining the spatial distribution of acetate.

In addition to the issue of competing for injected organic carbon, high sulfate concentration in the field also leads to a large possibility of pore clogging. After two successive years of biostimulation experiments (a total of 230 days of acetate amendment), the mineral precipitates and biomass are estimated to have reached up to 5.4% by volume of the pore space in the vicinity of injection wells. This represents a volume-averaged result for the 24.7 by 24.7 cm grid cell employed in the simulations. Although a maximum of 5.4% of

the pore space may seem small, the occurrence of pore clogging can depend very much on the characteristics of the sediments. With equal amounts of biomass, clogging can be much more pronounced in fine-textured materials than in coarse-textured ones (Vandevivere, 1995). Depending on the type of sediments, a small percentage of biomass can have large impact on the conductivity field and therefore the flow field. For example, in column experiments, Vandevivere and Baveye (1992) estimated biomass occupied 8.5% of the pore volume and Bielefeldt et al. (2002) estimated biomass occupied 3–8% of the pore space. Both studies indicated a reduction of hydraulic conductivity of up to three orders of magnitude. The large reduction of conductivity with the small amount of biomass accumulation may also be due to the nature of the biomass, which not only includes bacterial cells, but also viscous materials such as Extracellular Polymer Substance (EPS). These materials can reduce the flow-conducting volume and therefore clog the pore significantly (Hand et al., 2008). In addition, biomass can have a different morphology on the surface of solid phases, with the formation of discrete colonies easier to clog pores than biofilms (Thullner et al., 2002). As such, it is possible that 5.4% of pore volume reduction can lead to significant change in the conductivity field.

Comparison between predictions from the 1D homogeneous system and the 2D heterogeneous system shows that a homogeneous system can overestimate the amount of FeRB accumulation, as well as the rates and extent of iron depletion. This is because iron reduction requires the coexistence of both Fe(III) and acetate. In the heterogeneous case, the negative correlation between Fe(III) content and hydraulic conductivity leads to preferred flow paths that bypass regions of high Fe(III) content. For sulfate reducers, however, a homogeneous system can adequately capture the average behavior of the SRB, indicating the much smaller impact of heterogeneities on the sulfate reducing processes. Nonetheless, the heterogeneities of the subsurface can lead to localized high accumulation of biomass and precipitates from sulfate-reducing reactions, leading to a much higher possibility of pore clogging. The 1D homogeneous case predicts a maximum of overall 1.5 vol.% reduction of the pore space by the biomass and precipitates, while the 2D heterogeneous system predicts a maximum of 5.4 vol.% reduction of pore space.

It is surprising that the 1D homogeneous system adequately predicts the total amount of the reduced uranium. This may be due to the fact that, similar to sulfate, uranium also exists ubiquitously and has a continuous supply from up-gradient. It may be also due to the fact that there was a significant amount of bioavailable Fe(III) in the vicinity of the injection wells (Fig. 2B), which eventually led to a sufficient amount of FeRB covering across the line of the injection wells (Fig. 7B–C). If Fe(III) were more limited in the vicinity of the injection wells and FeRB only grew in part of the injection well vicinity regions, the situation could be quite different. As such, it is quite possible that the spatial distribution of the Fe(III) in the vicinity of the injection wells plays a key role in determining the overall efficacy of uranium immobilization.

To the best of our knowledge, this is the first field scale research that assesses the role of physical and geochemical heterogeneities in determining the spatial and temporal evolution of the reaction products associated with field scale

bioremediation, utilizing aqueous geochemistry and mineral characterization data to constrain the model. While the work illustrates the power of reactive transport models to "reproduce" what occurred in the field based on data and to quantify the evolution of reaction products, it is inevitable that the exercise is characterized by a certain level of uncertainty due to the complex nature of the field site, the multiple processes involved, as well as the scarcity of the field data. For example, the calculations presented here are based on hydraulic conductivity and Fe(III) fields that were generated based on the field data and an assumed inverse relationship between the two. Although it is qualitatively supported by the characterization date of the sediments, it is not certain to what extent these two variables are negatively correlated. This could introduce uncertainty in the estimation of mineral precipitates and biomass. The extent of uncertainty is being evaluated and is the topic of another manuscript. Further uncertainty is introduced by the fact that the modeling presented in this study did not include feedbacks between the formation of precipitates and biomass and the change in the hydraulic conductivity field due to pore clogging. Implementation of these feedbacks into the reactive transport simulations of bioremediation at the site is part of our ongoing research.

5. Summary

We simulated the transport and biogeochemical processes that occurred during field biostimulation experiments using a combination of inverse transport and reactive transport modeling. Validated by the best fit to the field data, we then evaluated the effects of physical and geochemical heterogeneities on the spatial distributions of mineral precipitates and biomass that has accumulated during the experiments. We draw the following conclusions:

- A maximum amount of mineral precipitates and biomass occur in the vicinity of the injection wells, reaching up to 5.4 vol.% of the pore space.
- Accumulation close to the injection wells is dominated by precipitates and biomass from the sulfate reducing reaction and is not strongly affected by physical and geochemical heterogeneities because of the ubiquitous presence of sulfate in the groundwater.
- Precipitates and biomass in the down-gradient regions are primarily reaction products associated with the iron-reducing reaction, the spatial patterns of which are strongly controlled by both physical and geochemical heterogeneities.
- The extent to which subsurface heterogeneities play a role is determined by the ratio of electron donors and mobile versus immobile acceptors on an electron-equivalent basis. The ubiquitous existence of high concentration mobile electron acceptors can "disguise" (or limit) the effects of subsurface heterogeneities.
- Heterogeneities result in localized larger accumulation of biomass and precipitates, leading to a greater possibility of pore clogging.
- The assumption of homogeneity can lead to an overestimation of FeRB accumulation, as well as the rate and extent of iron depletion. However, it can adequately capture the average spatial distribution of the sulfate reducers and the total amount of bioreduced uranium.

Acknowledgements

References

Anderson, R.T., et al., 2003. Stimulating the in situ activity of Geobacter species to remove uranium from the groundwater of a uranium-contaminated aquifer. Appl. Environ. Microb. 69 (10), 5884–5891.

Barber, L.B., Thurman, E.M., Runnells, D.D., 1992. Geochemical heterogeneity in a sand and gravel aquifer — effect of sediment mineralogy and particle-size on the sorption of chlorobenzenes. J. Contam. Hydrol. 9 (1–2), 35–54.

Baveye, P., Vandevivere, P., Hoyle, B.L., DeLeo, P.C., de Lozada, D.S., 1998. Environmental impact and mechanisms of the biological clogging of saturated soils and aquifer materials. Crit. Rev. Env. Sci. Tec. 28 (2), 123–191.

Bielefeldt, A.R., McEachern, C., Illangasekare, T., 2002. Hydrodynamic changes in sand due to biogrowth on naphthalene and decane. J. Environ. Eng.-ASCE. 128 (1), 51–59.

Bonneville, S., Van Cappellen, P., Behrends, T., 2004. Microbial reduction of iron (III) oxyhydroxides: effects of mineral solubility and availability. Chem. Geol. 212 (3–4), 255–268.

Boonchayaanant, B., Kitanidis, P.K., Criddle, C.S., 2008. Growth and cometabolic reduction kinetics of a uranium- and sulfate-reducing Desulfovibrio Clostridia mixed culture: temperature effects. Biotechnol. Bioeng. 99 (5), 1107–1119.

Charlet, L., Tournassat, C., 2005. Fe(II)–Na(I)–Ca(II) cation exchange on montmorillonite in chloride medium: evidence for preferential clay adsorption of chloride — metal ion pairs in seawater. Aquat. Geochem. 11 (2), 115–137.

Cord-Ruwisch, R., Lovley, D.R., Schink, B., 1998. Growth of Geobacter sulfurreducens with acetate in syntrophic cooperation with hydrogen-oxidizing anaerobic partners. Appl. Environ. Microb. 64 (6), 2232–2236.

Cunningham, A.B., Characklis, W.G., Abedeen, F., Crawford, D., 1991. Influence of biofilm accumulation on porous-media hydrodynamics. Environ. Sci. Technol. 25 (7), 1305–1311.

Dagan, G., 1990. Transport in heterogeneous porous formations — spatial moments, ergodicity, and effective dispersion. Water Resour. Res. 26 (6), 1281–1290.

de Marsily, G., et al., 2005. Dealing with spatial heterogeneity. Hydrogeol. J. 13 (1), 161–183.

Deutsch, C.V., Journel, A.G., 1992. GSLIB: Geostatistical Software Library and User's Guide (Applied Geostatistics Series). Oxford University Press, Inc., New York, 369 pp.

Englert, A., Hubbard, S.S., Williams, K.H., Li, L, Steefel, C.I., 2009. Feedbacks between hydrological heterogeneity and bioremediation induced biogeochemical transformations. Environ. Sci. Technol. doi:10.1021/es803367n.

Englert, A., Kowalsky, M.B. and Hubbard, S.S., in preparation. Characterization of field scale transport behavior during stimulated bioremediation. J. Hydrol.

Esteve-Núñez, A., Rothermich, M., Sharma, M., Lovley, D., 2005. Growth of *Geobacter sulfurreducens* under nutrient-limiting conditions in continuous culture. Environ. Microb. 7 (5), 641–648.

Faybishenko, B., et al., 2008. In situ long-term reductive bioimmobilization of Cr(VI) in groundwater using hydrogen release compound. Environ. Sci. Technol. 42 (22), 8478–8485.

Finsterle, S., 2004. Multiphase inverse modeling: review and iTOUGH2 applications. Vadose Zone J. 3 (3), 747–762.

Freeze, R.A., 1975. A stochastic-conceptual analysis of one-dimensional groundwater flow in nonuniform homogeneous media. Water Resour. Res. 11, 725–741.

Gelhar, L.W., 1993. Stochastic subsurface hydrology. Prentice-Hall, Englewood Cliffs, N.J. 390 pp.

Gelhar, L.W., Axness, C.L., 1983. Three-dimensional stochastic analysis of macrodispersion in aquifers. Water Resour. Res. 19 (1), 161–180.

Gelhar, L.W., Welty, C., Rehfeldt, K.R., 1992. A critical-review of data on field-scale dispersion in aquifers. Water Resour. Res. 28 (7), 1955–1974.

Giambalvo, E.R., Steefel, C.I., Fisher, A.T., Rosenberg, N.D., Wheat, C.G., 2002. Effect of fluid-sediment reaction on hydrothermal fluxes of major elements, eastern flank of the Juan de Fuca Ridge. Geochim. Cosmochim. Acta 66 (10), 1739–1757.

Glassley, W.E., Simmons, A.M., Kercher, J.R., 2002. Mineralogical heterogeneity in fractured, porous media and its representation in reactive transport models. Appl. Geochem. 17 (6), 699–708.

Gomez-Hernandez, J.J., Sahuquillo, A., Capilla, J.E., 1997. Stochastic simulation of transmissivity fields conditional to both transmissivity and piezometric data—1, Theory. J. Hydrol. 203, 162–174.

Griebler, C., Mindl, B., Slezak, D., Geiger-Kaiser, M., 2002. Distribution patterns of attached and suspended bacteria in pristine and contaminated shallow aquifers studied with an in situ sediment exposure microcosm. Aquat. Microb. Ecol. 28 (2), 117–129.

Hand, V.L., Lloyd, J.R., Vaughan, D.J., Wilkins, M.J., Boult, S., 2008. Experimental studies of the influence of grain size, oxygen availability and organic carbon availability on bioclogging in porous media. Environ. Sci. Technol. 42 (5), 1485–1491.

Jung, J., Hyun, S.P., Lee, J.K., Cho, Y.H., Hahn, P.S., 1999. Adsorption of UO22+ on natural composite materials. J. Radioanal. Nucl. Chem. 242 (2), 405–412.

Knauss, K.G., Johnson, J.W., Steefel, C.I., 2005. Evaluation of the impact of CO_2, co-contaminant gas, aqueous fluid and reservoir rock interactions on the geologic sequestration of CO_2. Chem. Geol. 217, 339–350.

Komlos, J., Kukkadapu, R.K., Zachara, J.M., Jaffe, P.R., 2007. Biostimulation of iron reduction and subsequent oxidation of sediment containing Fe-silicates and Fe-oxides: effect of redox cycling on Fe(III) bioreduction. Water Res. 41 (13), 2996–3004.

Kowalsky, M.B., et al., 2005. Estimation of field-scale soil hydraulic and dielectric parameters through joint inversion of GPR and hydrological data. Water Resour. Res. 41 (W11425). doi:10.1029/2005WR004237.

Kowalsky, M.B., Finsterle, S., Rubin, Y., 2004. Estimating flow parameter distributions using ground-penetrating radar and hydrological measurements during transient flow in the vadose zone. Adv. Water Resour. 27 (6), 583–599.

Lasaga, A.C., 1998. Kinetic theory in the earth sciences. Princeton Series in Geochemistry. Princeton University Press, Princeton. 811 pp.

Li, L., Peters, C.A., Celia, M.A., 2006. Upscaling geochemical reaction rates using pore-scale network modeling. Adv. Water Resour. 29 (9), 1351–1370.

Li, L., Peters, C.A., Celia, M.A., 2007a. Applicability of averaged concentrations in determining geochemical reaction rates in heterogeneous porous media. Am. J. Sci. 307, 1146–1166.

Li, L., Peters, C.A., Celia, M.A., 2007b. Effects of mineral spatial distribution on reaction rates in porous media. Water Resour. Res. 43 (1). doi:10.1029/2005WR004848.

Li, L, Steefel, C.I., Williams, K.H., Wilkins, M.J., Hubbard, S.S., 2009. Mineral transformation and biomass accumulation during uranium bioremediation at Rifle, Colorado. Environ. Sci. Technol. 43 (14), 5429–5435. doi:10.1021/es900016v.

Liu, C.X., Kota, S., Zachara, J.M., Fredrickson, J.K., Brinkman, C.K., 2001. Kinetic analysis of the baterial reduction of goethite. Environ. Sci. Technol. 35 (12), 2482–2490.

Lichtner, P.C., 1985. Continuum model for simultaneous chemical-reactions and mass-transport in hydrothermal systems. Geochim. Cosmochim. Acta 49 (3), 779–800.

Lloyd, J.R., 2003. Microbial reduction of metals and radionuclides. FEMS Microb. Rev. 27 (2–3), 411–425.

Loferer-Krossbacher, M., Klima, J., Psenner, R., 1998. Determination of bacterial cell dry mass by transmission electron microscopy and densitometric image analysis. Appl. Environ. Microb. 64 (2), 688–694.

Lovley, D.R., Phillips, E.J.P., 1987. Rapid assay for microbially reducible ferric iron in aquatic sediments. Appl. Environ. Microb. 53 (7), 1536–1540.

Lovley, D.R., Phillips, E.J.P., 1992. Bioremediation of uranium contamination with enzymatic uranium reduction. Environ. Sci. Technol. 26 (11), 2228–2234.

Lovley, D.R., Phillips, E.J.P., Gorby, Y.A., Landa, E.R., 1991. Microbial reduction of uranium. Nature 350 (6317), 413–416.

Luo, J., et al., 2007. Modeling in-situ uranium(VI) bioreduction by sulfate-reducing bacteria. J. Contam. Hydrol. 92 (1–2), 129–148.

Mahadevan, R., et al., 2006. Characterization of metabolism in the Fe(III)-reducing organism Geobacter sulfurreducens by constraint-based modeling. Appl. Environ. Microb. 72 (2), 1558–1568.

Maher, K., Steefel, C.I., DePaolo, D.J., Viani, B.E., 2006. The mineral dissolution rate conundrum: insights from reactive transport modeling of U isotopes and pore fluid chemistry in marine sediments. Geochim. Cosmochim. Acta 70 (2), 337–363.

Meile, C., Tuncay, K., 2006. Scale dependence of reaction rates in porous media. Adv. Water Resour. 29 (1), 62–71.

Molins, S., Mayer, K.U., 2007. Coupling between geochemical reactions and multicomponent gas and solute transport in unsaturated media: a reactive transport modeling study. Water Resour. Res. 43 (5).

Monod, J., 1949. The growth of bacterial cultures. Ann. Rev. Microbiol. 3, 371–394.

Pallud, C., Van Cappellen, P., 2006. Kinetics of microbial sulfate reduction in estuarine sediments. Geochim. Cosmochim. Acta 70 (5), 1148–1162.

Porter, D., Roychoudhury, A.N., Cowan, D., 2007. Dissimilatory sulfate reduction in hypersaline coastal pans: activity across a salinity gradient. Geochim. Cosmochim. Acta 71 (21), 5102–5116.

Pruess, K., Oldenburg, C., Moridis, G., 1999. TOUGH2 User's Guide, Version 2.0, Lawrence Berkeley National Laboratory Report LBNL-43134. Berkeley, CA.

Rittmann, B.E., McCarty, P.L., 2001. Environmental biotechnology: principles and applications. McGraw-Hill, New York.

Roden, E.E., Zachara, J.M., 1996. Microbial reduction of crystalline iron(III) oxides: influence of oxide surface area and potential for cell growth. Environ. Sci. Technol. 30 (5), 1618–1628.

Ross, S.M., 2000. Introduction to Probability Models. Academic Press, San Diego, CA. xv, 693 pp.

Rutgers, M., van der Gulden, H.M.L., Dam, K., 1989. Thermodynamic efficiency of bacterial growth calculated from growth yield of Pseudomonas oxalaticus OX1 in the chemostat. Biochim. Biophys. Acta, Bioenerg. 973 (2), 302–307.

Scheibe, T.D., et al., 2006. Transport and biogeochemical reaction of metals in a physically and chemically heterogeneous aquifer. Geosphere 2 (4). doi:10.1130/GES00029.1.

Seki, K., Thullner, M., Hanada, J., Miyazaki, T., 2006. Moderate bioclogging leading to preferential flow paths in biobarriers. Ground Water Monit. R. 26 (3), 68–76.

Shelobolina, E.S., et al., 2004. Importance of clay size minerals for Fe(III) respiration in a petroleum-contaminated aquifer. Geobiology 2, 67–76.

Steefel, C.I., Maher, K., 2009. Fluid–rock interaction: a reactive transport approach. Rev. Mineral. Geochem. doi:10.2138/rmg.2009.70.11.

Taylor, S.W., Jaffe, P.R., 1990a. Biofilm growth and the related changes in the physical-properties of a porous-medium.1. Experimental investigation. Water Resour. Res. 26 (9), 2153–2159.

Taylor, S.W., Jaffe, P.R., 1990b. Biofilm growth and the related changes in the physical-properties of a porous-medium. 3. Dispersivity and model verification. Water Resour. Res. 26 (9), 2171–2180.

Thullner, M., Zeyer, J., Kinzelbach, W., 2002. Influence of microbial growth on hydraulic properties of pore networks. Transport Porous Med. 49 (1), 99–122.

Tompson, A.F.B., Schafer, A.L., Smith, R.W., 1996. Impacts of physical and chemical heterogeneity on cocontaminant transport in a sandy porous medium. Water Resour. Res. 32 (4), 801–818.

Van Cappellen, P., Wang, Y.F., 1996. Cycling of iron and manganese in surface sediments: a general theory for the coupled transport and reaction of carbon, oxygen, nitrogen, sulfur, iron, and manganese. Am. J. Sci. 296, 197–243.

VanBriesen, J.M., 2002. Evaluation of methods to predict bacterial yield using thermodynamics. Biodegradation 13 (3), 171–190.

Vandevivere, P., 1995. Bacterial clogging of porous-media — a new modeling approach. Biofouling 8 (4), 281–291.

Vandevivere, P., Baveye, P., 1992. Relationship between Transport of Bacteria and Their Clogging Efficiency in Sand Columns. Appl. Environ. Microb. 58 (8), 2523–2530.

Vrionis, H.A., et al., 2005. Microbiological and geochemical heterogeneity in an in situ uranium bioremediation field site. Appl. Environ. Microb. 71 (10), 6308–6318.

Wang, S., Jaffe, P.R., Li, G., Wang, S.W., Rabitz, H.A., 2003. Simulating bioremediation of uranium-contaminated aquifers; uncertainty assessment of model parameters. J. Contam. Hydrol. 64 (3–4), 283–307.

Wu, W.M., et al., 2006. Pilot-scale in situ bioremediation of uranium in a highly contaminated aquifer. 1. Conditioning of a treatment zone. Environ. Sci. Technol. 40 (12), 3978–3985.

Yabusaki, S.B., et al., 2007. Uranium removal from groundwater via in situ biostimulation: field-scale modeling of transport and biological processes. J. Contam. Hydrol. 93 (1–4), 216–235.

Yao, W.S., Millero, F.J., 1996. Oxidation of hydrogen sulfide by hydrous Fe(III) oxides in seawater. Mar. Chem. 52 (1), 1–16.

Zachara, J.M., Gassman, P.L., Smith, S.C., Taylor, D., 1995. Oxidation and adsorption of Co(II)EDTA(2−) complexes in subsurface materials with iron and manganese oxide grain coatings. Geochim. Cosmochim. Acta 59 (21), 4449–4463.

Zinn, B., et al., 2004. Experimental visualization of solute transport and mass transfer processes in two-dimensional conductivity fields with connected regions of high conductivity. Environ. Sci. Technol. 38 (14), 3916–3926.